Neuron

NeuroResource

A bimodal taxonomy of adult human brain sulcal morphology related to timing of fetal sulcation and trans-sulcal gene expression gradients

Graphical abstract

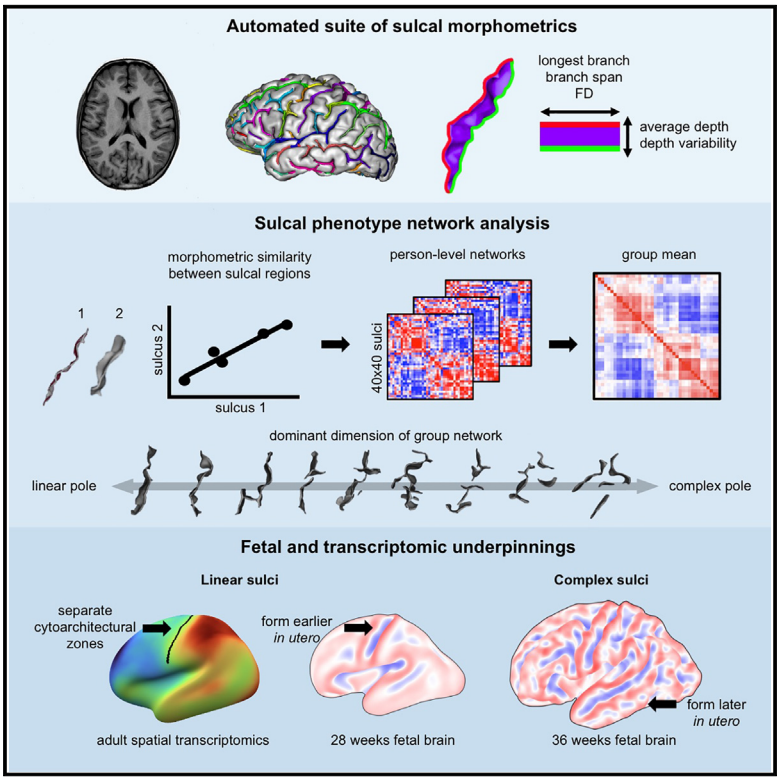

Highlights

- A pipeline is provided to extract 5 phenotypes for each of 40 sulci from brain MRI
- Sulcal phenotype networks consistently find an axis of linear to complex shape
- Adult sulcal complexity is linked to heritability, function, and fetal sulcation
- Linear sulci demarcate zones of expression for developmentally enriched genes

Authors

William E. Snyder, Petra E. Vértes, Vanessa Kyriakopoulou, ..., Jean-Francois Mangin, Armin Raznahan, Edward T. Bullmore

Correspondence

will.snyder@nih.gov

In brief

Snyder et al. develop measures of human cortical folding, revealing an axis of linear to complex sulcal shape across the adult cortex. This axis predicts the phased emergence of sulci *in utero* and boundaries of cortical gene expression, implicating these processes in the formation of mature cortical geometry.

Snyder et al., 2024, Neuron *112*, 3396–3411
October 23, 2024 Published by Elsevier Inc.
https://doi.org/10.1016/j.neuron.2024.07.023

CellPress

CellPress
OPEN ACCESS

Neuron

NeuroResource

A bimodal taxonomy of adult human brain sulcal morphology related to timing of fetal sulcation and trans-sulcal gene expression gradients

William E. Snyder,[1,2,14,*] Petra E. Vértes,[1] Vanessa Kyriakopoulou,[3,4] Konrad Wagstyl,[5] Logan Z.J. Williams,[3,4] Dustin Moraczewski,[6] Adam G. Thomas,[6] Vyacheslav R. Karolis,[3,7] Jakob Seidlitz,[8,9,10] Denis Rivière,[11] Emma C. Robinson,[3,4] Jean-Francois Mangin,[11] Armin Raznahan,[2,13] and Edward T. Bullmore[1,12,13]

[1]Department of Psychiatry, University of Cambridge, Cambridge, UK
[2]Section on Developmental Neurogenomics, Human Genetics Branch, National Institute of Mental Health Intramural Research Program, Bethesda, MD, USA
[3]Centre for the Developing Brain, School of Biomedical Engineering and Imaging Sciences, King's College London, London, UK
[4]Department of Biomedical Engineering, School of Biomedical Engineering and Imaging Science, King's College London, London, UK
[5]Wellcome Centre for Human Neuroimaging, University College London, London, UK
[6]Data Science and Sharing Team, National Institute of Mental Health, Bethesda, MD, USA
[7]Wellcome Centre for Integrative Neuroimaging, FMRIB, Nuffield Department of Clinical Neurosciences, University of Oxford, Oxford, UK
[8]Lifespan Brain Institute, Children's Hospital of Philadelphia, University of Pennsylvania, Philadelphia, PA, USA
[9]Department of Psychiatry, University of Pennsylvania, Philadelphia, PA, USA
[10]Department of Child and Adolescent Psychiatry and Behavioral Science, The Children's Hospital of Philadelphia, Philadelphia, PA, USA
[11]Université Paris-Saclay, CEA, CNRS, Neurospin, Baobab, Gif-sur-Yvette 91191, France
[12]Cambridgeshire & Peterborough NHS Foundation Trust, Cambridge, UK
[13]These authors contributed equally
[14]Lead contact
*Correspondence: will.snyder@nih.gov
https://doi.org/10.1016/j.neuron.2024.07.023

SUMMARY

We developed a computational pipeline (now provided as a resource) for measuring morphological similarity between cortical surface sulci to construct a sulcal phenotype network (SPN) from each magnetic resonance imaging (MRI) scan in an adult cohort (n = 34,725; 45–82 years). Networks estimated from pairwise similarities of 40 sulci on 5 morphological metrics comprised two clusters of sulci, represented also by the bimodal distribution of sulci on a linear-to-complex dimension. Linear sulci were more heritable and typically located in unimodal cortex, and complex sulci were less heritable and typically located in heteromodal cortex. Aligning these results with an independent fetal brain MRI cohort (n = 228; 21–36 gestational weeks), we found that linear sulci formed earlier, and the earliest and latest-forming sulci had the least between-adult variation. Using high-resolution maps of cortical gene expression, we found that linear sulcation is mechanistically underpinned by trans-sulcal gene expression gradients enriched for developmental processes.

INTRODUCTION

The adult human brain has a complex surface of grooves (sulci) and ridges (gyri). The cerebral cortex forms embryonically from distension of the neural tube, and its surface remains smooth (lissencephalic) until about 20 weeks gestational age (GA) in humans.[1,2] In the second half of pregnancy, the cortical sheet becomes progressively more wrinkled (gyrencephalic) as more sulci indent its surface.[3–5] At birth, the sulco-gyral patterning of the brain is thought to be close to its life-long final configuration,[6–8] as complexly patterned and individually unique as the fingerprints that are also enduringly formed at birth.[9] However, it has been challenging to quantify such a spatio-temporally complex and individually variable process as human brain cortical surface patterning.

In existing sulcal taxonomies, expert but largely qualitative postmortem examinations of limited quantities of human brains have supported the classification of adult sulci into two or three categories or classes, linked to their timing of fetal emergence or sulcation.[3,4] These classifications—into primary, secondary, or tertiary sulci—have been defined differently across studies but can converge on notions of time of sulcal emergence, hierarchical relationships in sulcal size, and phylogenetic presentation.[3,10,11] Sulci consistently classified as primary, like the central sulcus, are the first and longest sulci to form and are conserved in shape across primates.[12] In humans, primary sulci begin to

CellPress
OPEN ACCESS

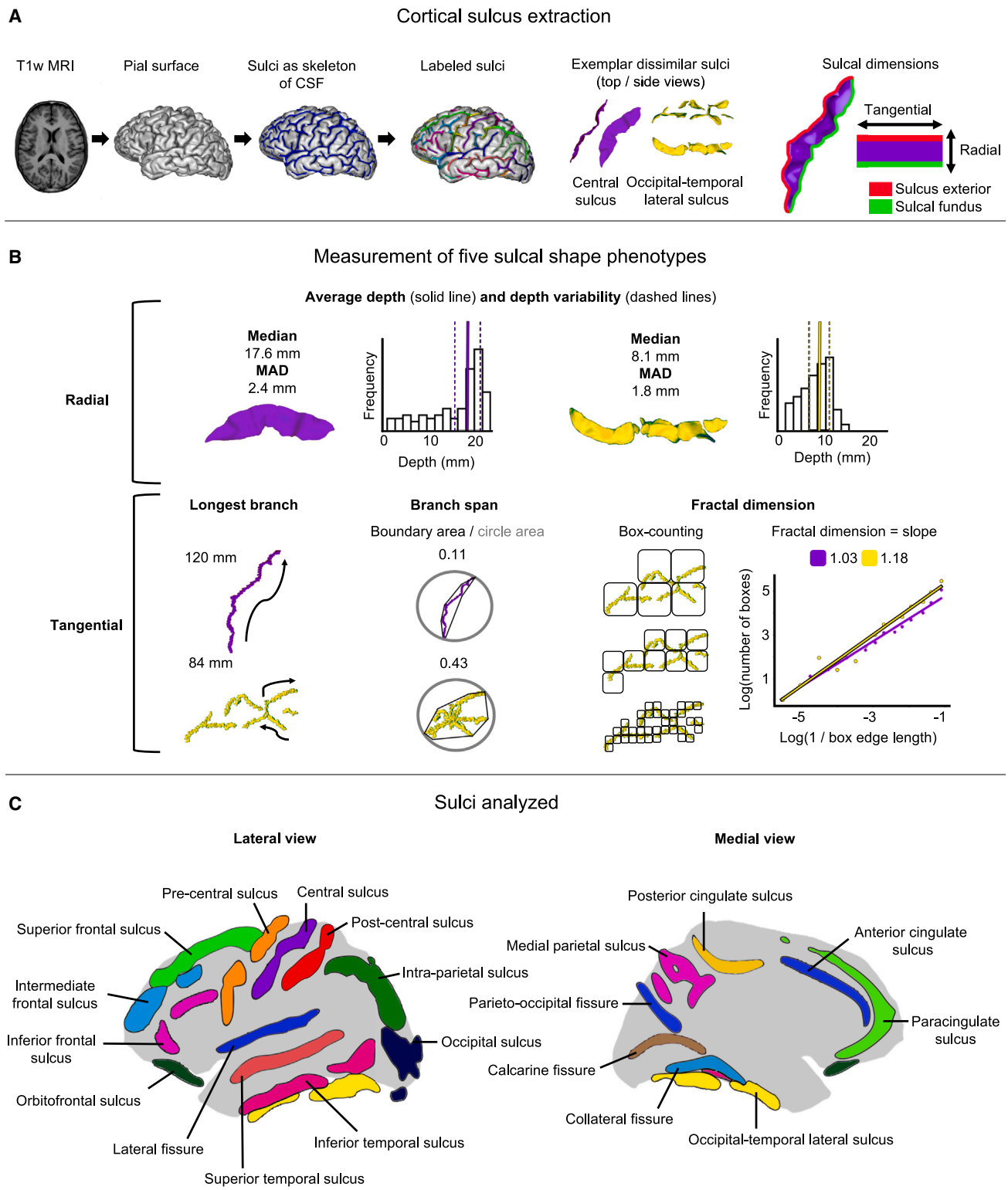

Figure 1. A suite of sulcal morphometrics spanning radial and tangential dimensions

(A) 20 sulci per brain hemisphere were segmented and labeled in each of 34,725 adult brain MRI scans. Sulci were measured along the dimensions radial (from sulcal fundus to sulcus exterior) or tangential to the cortex (along the sulcus exterior).

(B) Five shape metrics were measured for each sulcus. Two metrics measured radial dimensions: average depth of the sulcal floor and variability of the depth along the length of the sulcus. Three metrics measured tangential dimensions: the length of the longest branch, branch span, and fractal dimension (FD). Depth

(legend continued on next page)

appear in the second trimester of pregnancy, from about 20 weeks GA, until ~32 weeks GA (early third trimester). Secondary sulci are sometimes defined as the more variable branches from primary sulci[3,8] and emerge between ~32 and 38 weeks GA. The few tertiary sulci similarly emerge after 38 weeks and for some months post-natally.[2,3] However, this primary-to-tertiary labeling model remains quite arbitrary with considerable uncertainty over the correct labeling for many sulci (e.g., the middle frontal sulcus is labeled differently in Chi et al.,[3] Dubois et al.,[8] and Voorhies et al.[13]). Fundamentally, our understanding of sulcal complexity and its fetal ontogenesis has been limited by the scale and quantitative scope of postmortem brain studies.

The advent of computational methods for sulcal morphometry from magnetic resonance imaging (MRI) data, e.g., BrainVISA's Morphologist toolbox (http://brainvisa.info),[14–16] has advanced the field by standardizing and automating sulcal segmentation, enabling fully quantitative assessments of sulcal shape. Geometric measurements, such as sulcal surface area and depth, are heritable,[17,18] related to cognition,[13,19] and related to psychiatric and neurodevelopmental disorders.[18,20] Measures driven by sulcal patterning such as global and local gyrification,[21–23] as well as cortical surface area and curvature,[24,25] also highlight sulcal patterning's importance in health and disorder. Although there is increasing interest in measuring the similarity of cortical areas in terms of multiple MRI measures of geometry and tissue composition, using methods like morphometric similarity network (MSN) analysis,[26] there have been very limited comparable investigations of systemic patterns of covariation between sulci in terms of their size and shape metrics. Additionally, recent advances in analysis of complex sulcal anatomy from adult MRI scans have not yet been linked to insights into the fetal developmental timing of sulcation.

In this context, we integrate two complementary technical innovations to define a new taxonomy of human cortical sulcation: (1) sulcal phenotype network (SPN) analysis of adult brain MRI in the UK Biobank[27,28] and (2) sulcal growth curve modeling of fetal brains from the Developing Human Connectome Project (dHCP).[29] We show that this new taxonomy of cortical sulcation in adulthood can be linked to the timing of brain sulcation in development and is coupled with diverse facets of multiscale cortical organization. Transcriptomic analysis allowed us to examine the mechanistic hypothesis that the most heritable, earliest-forming, linear sulci form at the boundaries between cytoarchitectonically differentiated cortical areas. Our resource provides containerized code for automated measure of an expanded suite of sulcal morphometrics. This suite allows for novel assessment of inter-regional differences in sulcal complexity that reflect maturationaly preserved features of the human cortical fingerprint. Together, our analyses comprise a resource of benchmark data for normative adult sulcal anatomy and fetal sulcal emergence, gene-level transcriptional annotation of sulci, and other adult maturational and functional annotation of sulci to enable future works to recognize and integrate our new taxonomy in fetal and adult human neuroscience.

RESULTS

Sample

Adult brain structural MRI (sMRI) data were obtained from the second release of the UK Biobank sMRI cohort.[27,28] A single sMRI scan was available for each of $n \sim 39{,}000$ participants (mean age = 64 years; 47% male) and was processed with FreeSurfer (http://surfer.nmr.mgh.harvard.edu/)[30,31] and BrainVISA Morphologist (http://brainvisa.info)[14–16] software. After excluding participants with neurological diagnoses[32] (n = 1,568) and scans that did not pass quality control (n = 2,247; see STAR Methods), we retained an analyzable sample of n = 34,725 scans (mean age = 64 years; age range = 45–82 years; 46% male) (Figure S1).

Fetal brain sMRI data were collected and processed with the dHCP (https://www.developingconnectome.org/) structural pipeline.[29,33] A total of n = 228 fetuses aged 21–36 gestational weeks were scanned *in utero* (Figure S1) and passed quality control for reconstruction of the inner cortical surfaces bilaterally (STAR Methods).

Sulcal phenotypes

For each adult brain scan, we segmented and labeled 40 sulci (20 per cerebral hemisphere [Figure 1A], see nomenclature in Figure 1C, elaborated in Figure S2) and estimated 5 shape metrics or features for each sulcus (Figure 1B): average (median) and variability (median absolute deviation [MAD]) of sulcal depth, longest branch length, branch span, and fractal dimension (FD). These five measures were chosen to encompass morphometric variation both tangential and radial to the cortical surface. Prior studies have examined these features in isolation from each other[3,13,19,34–39] but have not harnessed them as a combined group that can collectively triangulate the complex topography of any given sulcus.

Plots of average sulcal phenotypes had similar cortical patterning across phenotypes (Figure 2A), indicating coordination between phenotypes within subjects. The {1 × 40} feature vectors describing each phenotype's distribution across 40 sulci within an individual brain were correlated between the five sulcal

metrics were based on depth histograms, computed as the distance between points along the bottom of a sulcal valley (sulcal fundus) to the enclosing surface encompassing gyral peaks. The median estimated central location and the median absolute deviation (MAD) estimated variability. The length of the longest branch was the maximum geodesic distance along any sulcal branch. Branch span was estimated by drawing a convex hull around each sulcus projected into 2D and calculating the ratio of the hull area to the area that circumscribes the hull, $0 <$ branch span < 1. More complex, densely branched sulci occupy more of the space and have higher branch span than more linear, sparsely branched sulci. FD was estimated by a box-counting algorithm: the sulcus was iteratively tiled with boxes of different sizes and the number of boxes occupied by the sulcus at each size was counted; then $\sim 1 <$ FD < 2 was estimated by gradient of the log-log linear relationship between the size of boxes and the number of occupied boxes. More linear sulci have FD close to the limit of a Euclidean line (1), and more branched or complex sulci have FD closer to the limit of a Euclidean plane (2).

(C) We display the anatomical standard for the sulcal nomenclature used throughout the study. Sulcal phenotypes were measured for each of these 40 sulcal regions (20 per hemisphere), which were delineated by BrainVISA sulcal recognition or by merged sulcal labels in the standard BrainVISA parcellation.
See also Figure S2.

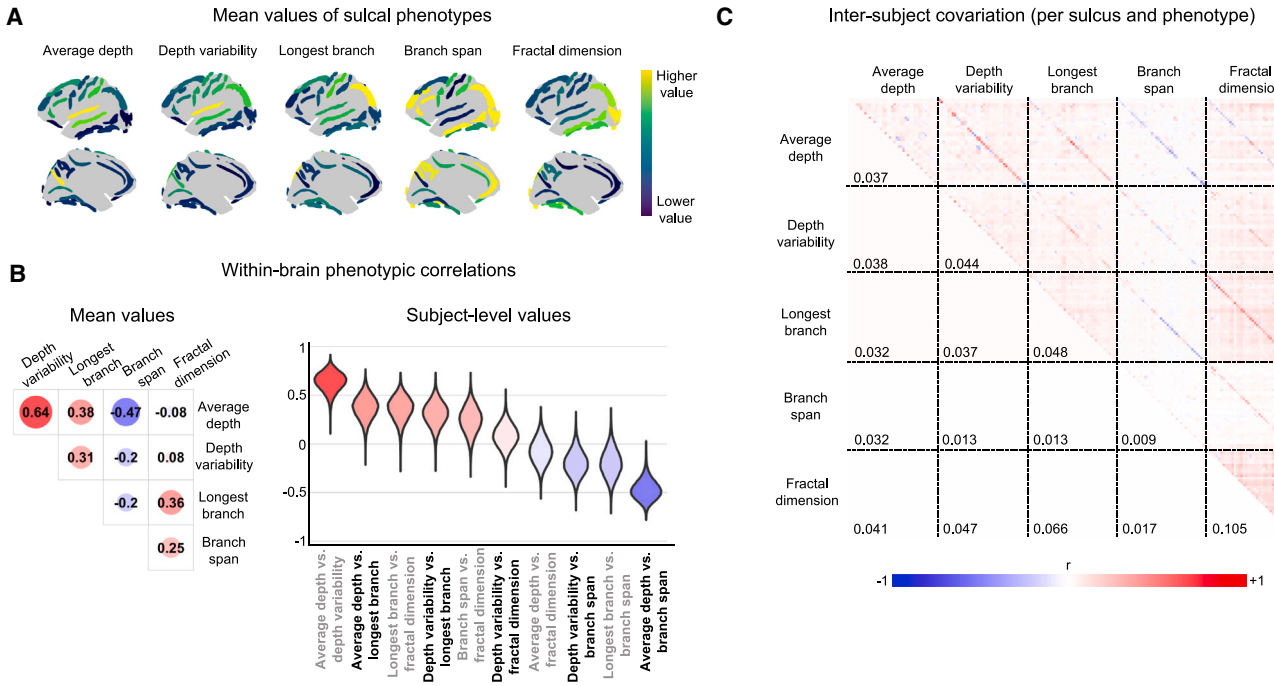

Figure 2. Cortical surface patterning of sulcal phenotypes and relationships between phenotypes

(A) Mean values of sulcal phenotypes are plotted to highlight relative differences between sulcal regions. Colors are shown on average sulci models, delineating their typical paths between gyri. The gradients of sulcal anatomy are similar across phenotypes, with sulci at the extremes of one phenotype often occupying extremes of other phenotypes.

(B) Average correlation between {1 × 40} sulcal phenotype vectors within brains in the adult UK Biobank dataset (left) and distribution of these correlations across individuals (right). Sulcal phenotypes exhibit a variety of inter-measure correlations, highlighting the shared and complementary information afforded by each feature.

(C) Between-subject sulcal covariation was low for any given set of sulci and sulcal phenotype (median absolute correlation = 0.03). Values on the lower triangle show the median absolute correlation between sulci across subjects for any set of two sulcal phenotypes. Diagonals within any given block represent the correlation between the same sulcus for two different phenotypes; the greater magnitude correlations along these diagonals are consistent with the idea that morphology is largely independent between sulci but forms by more consistent rules across phenotypes within a given sulcus.

See also Figures S3 and S5.

phenotypes and averaged across subjects. Average sulcal depth and depth variability were strongly positively correlated with each other and with the longest branch length, whereas branch span was negatively correlated with sulcal depth metrics and positively correlated with FD (Figure 2B, left). For example, the central sulcus and parieto-occipital fissure were both deep and linear in terms of low branch span and FD. These within-brain correlations were consistently expressed across subjects (Figure 2B, right).

Alternatively, sulcal covariation between subjects was measured as the correlation between the pair of {1 × 34,725} feature vectors representing a single phenotype, e.g., sulcal depth, at each of two sulci, e.g., central sulcus and lateral fissure average depth. In contrast to the strong covariation across folds within subjects, there was low covariation between folds across subjects (median absolute correlation = 0.03) (Figures 2C and S3A). This is in line with findings from Sun et al.[18] and is much less than the between-subject covariation observed with other commonly studied cortical phenotypes (Figure S3B). In exception, sulcal covariation across subjects was low but relatively higher between phenotypes for the same sulcus (block-wise diagonals in Figures 2C and S3A) (median absolute correlation = 0.17). Thus, it appears that different sulci show broadly reproducible morphological motifs across individuals (e.g., deep and linear vs. shallow and complex), but substantial individual differences in sulcal morphology result in generally low between-subject covariation.

SPNs reveal two dominant modes of sulcal morphology

To further investigate the similarity or dissimilarity between each pair of sulci in each adult brain, we estimated the {40 × 40} matrix of Pearson's correlations between the feature vectors of the same 5 metrics measured at each sulcus for each brain scan. This matrix was designated the SPN, with individual SPNs averaged to estimate the group mean SPN (Figure 3A; Table S1).

Hierarchical cluster analysis of the group mean SPN highlighted two large clusters of sulci that were positively correlated with (or similar to) other sulci in the same cluster and negatively correlated with (or dissimilar to) sulci in the other cluster (Figure 3B). The two clusters were also clearly differentiated in terms of the characteristic morphometry of their constituent sulci: one cluster, designated *linear*, comprised sulci with greater mean depth, variability of depth, and longest branch length; the other cluster, designated *complex*, comprised sulci with greater

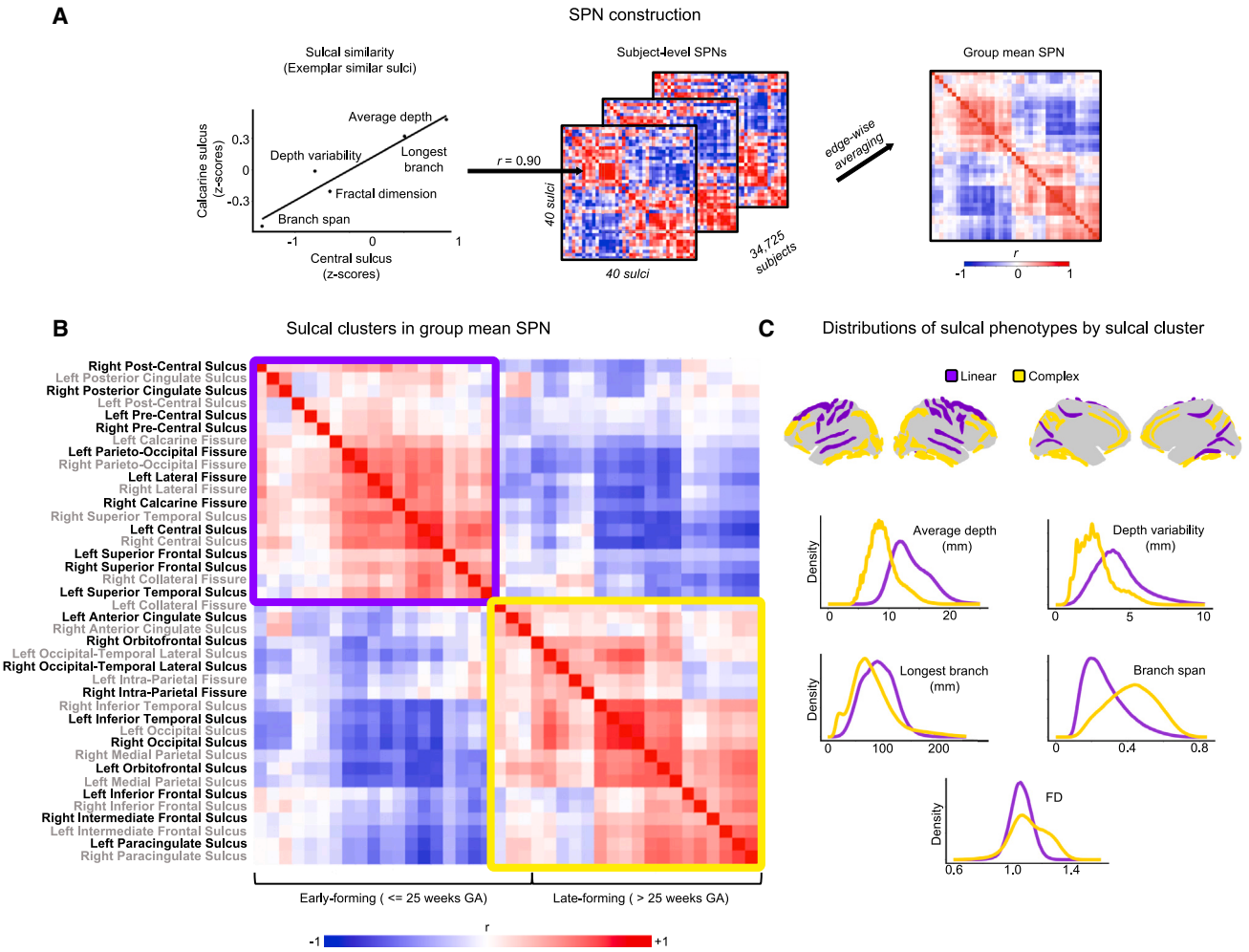

Figure 3. SPN analysis demonstrates that adult sulcal patterning is categorically represented by two major clusters, each comprising sulci that share distinctive (linear or complex) structural phenotypes

(A) Pearson's correlation between the five sulcal phenotypes measured at each pair of sulci (*Z* scored within each brain per metric) estimated the morphometric similarity of two sulci within the same brain. Repeated for each possible pair of 40 sulci, this analysis generated a {40 × 40} correlation matrix representing the similarity ($r > 0$) or dissimilarity ($r < 0$) of sulcal phenotypes across the cortex, and this was designated the SPN. Edge-wise averaging across subjects yielded the group mean SPN.

(B) The group mean SPN had two large clusters, separated almost entirely by early (≤25 weeks GA) and late (>25 weeks GA) forming sulci.

(C) The cluster termed "linear" was located in more central regions on the lateral and medial faces of the cortex with "complex" sulci situated at more extreme anterior, posterior, or ventral locations. Linear and complex names for sulcal clusters were based on the distinctive distribution of sulcal phenotypes displayed by each cluster, with the linear sulci having higher values in linear measures and complex sulci having higher values in fractal measures.

See also Figures S4 and S5 and Tables S1, S2, and S3.

branch span and FD (Figure 3C). Based on previous, postmortem labeling of when fetal sulci emerge,[3] we identified that the linear cluster's sulci formed almost exclusively by or before 25 weeks GA and the complex cluster's sulci formed almost exclusively after 25 weeks GA (Figure 3B). The clustering was further validated by the Dunn index, finding hierarchical clustering was maximized at a two-cluster solution (Figure S4A). SPN topology is highly consistent across subjects and robust to choice of subjects or sulci (Figures S4B–S4E); is robust to choice of included phenotypes or parcellation (Figure S4F); and has generally high test-retest reliability and high individual identifiability in retest scans (Figures S4G–S4I; Table S1). Despite small effects of age, sex, and total brain volume (TBV) on sulcal phenotypes and their covariation (Figures S3A, S5A, and S5B; Table S2), the structure of SPNs was overall invariant to these covariates (Figures S5B–S5D; Table S3). Given the technical robustness of the group mean SPN, we next explored its linear and complex patterning.

Sulci can be graded along a bimodal, linear-to-complex dimension that coheres with diverse gradients of cortical structure and function

We mapped the group mean SPN to a single, continuous dimension by computing its first principal component (PC)

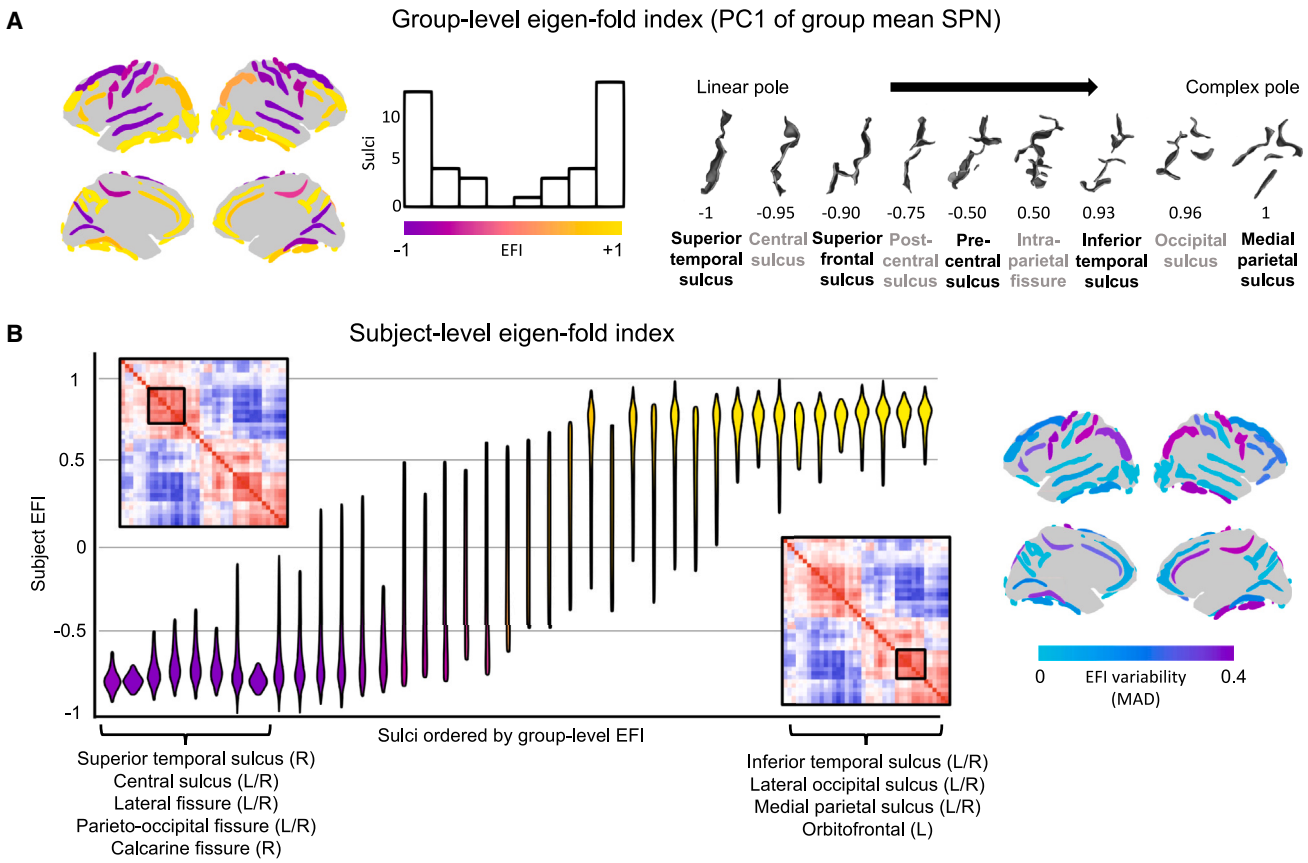

Figure 4. Adult sulcal patterning can be dimensionally represented by the eigen-fold index (EFI, first PC of the SPN) with both the most linear sulci (EFI ∼ –1) and the most complex sulci (EFI ∼ +1) having the lowest between-subject variability

(A) The EFI was derived as scaled values from PC1 of the group mean SPN, displaying a bimodal distribution with most weights for sulci at extreme ends of the dimension. Prototypical sulci were plotted in order from lowest to highest group-level EFI, depicting how this latent dimension captured linear to complex sulcal morphology.

(B) Subject-level EFI distributions for each sulcus were plotted, with distributions ordered from lowest to highest group-level EFI. Violin plots displayed the middle 80% of EFI distributions for each sulcus to highlight differences in the spread of EFI values. Sub-clusters from the group mean SPN are highlighted and were found to correspond to sulci with the lowest and highest ranking EFI values that also had the lowest inter-subject variability. Cortical patterning of inter-subject variability in sulcal complexity (MAD of EFI) demonstrated that sulci with high EFI variability could be directly adjacent to sulci with low EFI variability, such as with the pre/post-central sulcus adjacent to the central sulcus.

See also Table S1.

(Figure 4A; Table S1), which accounted for 27% of sulcal (co) variance across the cortex. Each sulcus was scored on the first PC, or eigen-fold index (EFI), and there was a clearly bimodal distribution of EFI scores (consistent with the two-cluster community structure), with most sulci scoring close to the linear (−1) or complex (+1) poles of the EFI and relatively few sulci having intermediate EFI scores (∼0). As shown for 10 illustrative examples, sulci with linear polar EFI scores were identifiably straighter and deeper than the more branched and fragmented sulci with complex polar EFI scores (Figure 4A). In these examples, it can be seen that linear sulci are dominantly composed of a single, primary sulcus, whereas more complex sulci exhibit additional secondary and tertiary branching.

The EFI score for each sulcus was also measured for each individual SPN, which provided a metric of inter-subject variability in the location of each sulcus on this bimodal, linear-to-complex dimension of sulcal morphometry (Figure 4B; Table S1; see STAR Methods). The correlation of subject EFI scores across subjects for any two sulci was low, just as with correlations from individual sulcal phenotypes (median absolute correlation = 0.04) but was generally higher for interhemispheric sulcal EFI correlations (median absolute correlation = 0.13). We found that the sulci that were closest to the linear pole (EFI score ∼ −1), and the sulci that were closest to the complex pole (EFI ∼ +1), had very low between-subject variability of EFI scores, whereas the sulci with less extreme EFI scores were markedly more variable between individual brain scans. The sulci with the most linear polar and most complex polar EFI scores formed separate sub-clusters within linear and complex clusters of the group mean SPN (Figure 4B). Between these poles, many other sulci varied widely between individuals in their position on the linear-to-complex spectrum of sulcal morphometry (Figure 4B). The greatest variability in EFI scores was seen for the left pre-central sulcus and left intra-parietal

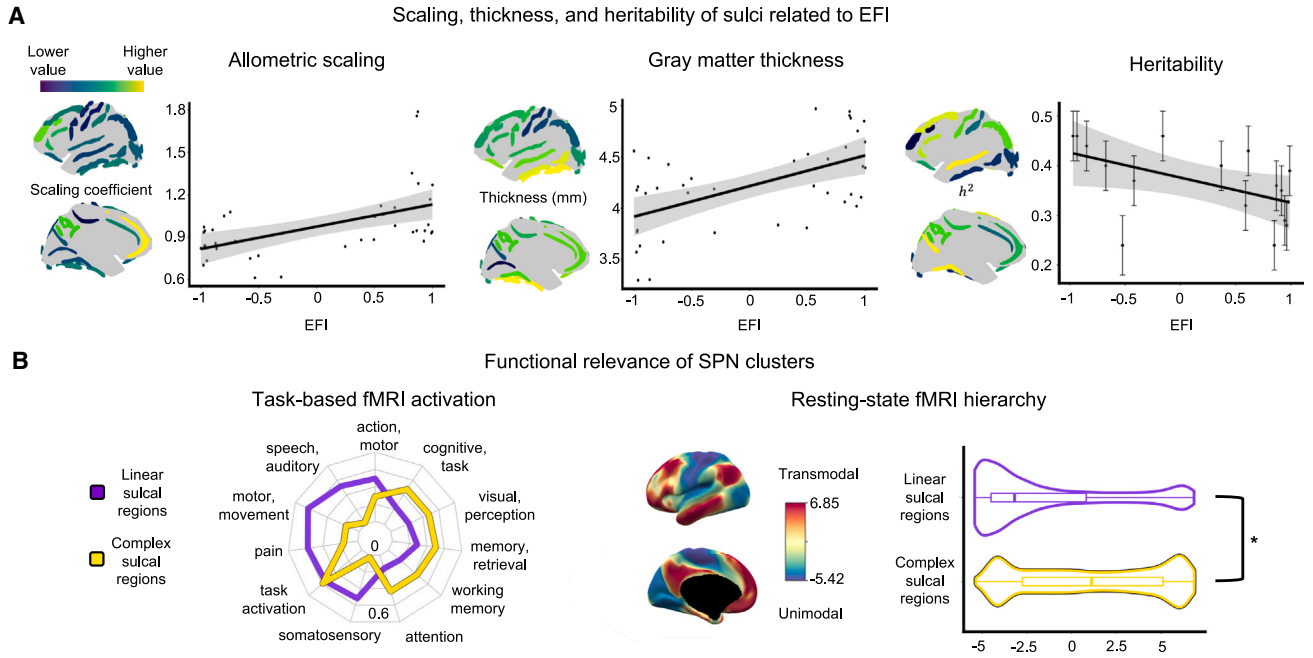

Figure 5. Dimensional (EFI) and categorical (SPN modular) metrics of sulcal patterning are related to cortical structure, heritability, and function

(A) Estimates of sulcal allometric scaling, gray matter thickness, and mean depth heritability were derived from BrainVISA sulcal morphometry, allowing direct comparison against EFI. Heritability estimates and their standard errors were available for a subset of displayed sulci (STAR Methods). EFI positively correlated with allometric scaling (r = 0.52, p = 0.00055) and gray matter thickness (r = 0.56, p = 0.00016) and negatively correlated with heritability (r = −0.514, p = 0.04). Therefore, deeper, more linear sulci were more heritable, located in thinner cortex, and received less disproportional expansion of surface area in larger brains. (B) SPN clusters were convergently distinguished by task and resting-state fMRI networks. Task-based functional annotations from Neurosynth revealed a sensorimotor to association bias from linear to complex sulci based on dice overlap. Resting-state functional connectivity (FC) gradients supported the relative enrichment of linear sulci for unimodal regions and of complex sulci for transmodal regions (p_{spin} = 0.0176).
See also Table S1.

fissure, suggesting that these folds are subject to the weakest developmental constraints relative to those folds at EFI poles. This "tethering" of the EFI at highly constrained poles meant that overall organization of sulcal morphology showed a highly stereotyped topography across individuals: the cross-sulcus correlation of individual EFI scores with the group-level EFI scores was strongly positive (mean = 0.78, standard deviation = 0.09).

Given such striking conservation of SPN clusters and the EFI axis across individuals, we hypothesized that the spatial ordering of folds by EFI score or SPN cluster would cohere with other recently described organizational axes of cortical structure and function.

We first sought to validate the EFI against independently derived descriptions of cortical structure based on BrainVISA metrics not included in SPN computation, including allometric scaling of sulcal surface area,[40–42] cortical thickness of areas adjacent to sulci,[43] and mean sulcal depth heritability[17] (STAR Methods; Figure 5A). These analyses revealed that: (1) EFI was positively correlated with brain-size dependent expansions of cortical surface area, i.e., cortical areas with more complex sulcal patterning had greatest relative surface area expansion with increasing brain size (Figure 5A, left); (2) EFI was positively correlated with cortical thickness, i.e., cortical areas adjacent to complex sulci were thicker than cortical areas intersected by linear sulci (Figure 5A, middle); and (3) EFI was negatively correlated with an independently generated estimate of sulcal depth heritability, i.e., linear sulci had greater heritability than more complex sulci (Figure 5A, right; all |r| > 0.5, p < 0.05). By contrast, inter-subject variability in EFI was not significantly correlated with sulcal depth heritability (r = −0.04).

We next compared SPN linear and complex clusters to functional MRI (fMRI) measures of cortical function during tasks and at rest (Figure 5B). Comparison with meta-analytic maps of task-related brain activation from over 11,000 fMRI studies (https://neurosynth.org)[44] revealed that cortical regions adjacent to linear sulci (EFI < 0) tend to be activated by somatosensory tasks, whereas regions adjacent to complex sulci (EFI > 0) are typically activated by higher-order cognitive and association tasks (Figure 5B, left). This functional differentiation of linear vs. complex folds was echoed by comparison with the topography of functional connectivity within the cortex at rest. Specifically, cortical areas surrounding linear and complex sulci, respectively, were differentiated in terms of their loadings on the sensory-to-association cortical gradient derived from diffusion map embedding of resting-state fMRI.[45] Cortical areas surrounding linear sulci had significantly lower (p_{spin} = 0.0176) functional connectivity gradient loadings, typical of unimodal cortex, compared with

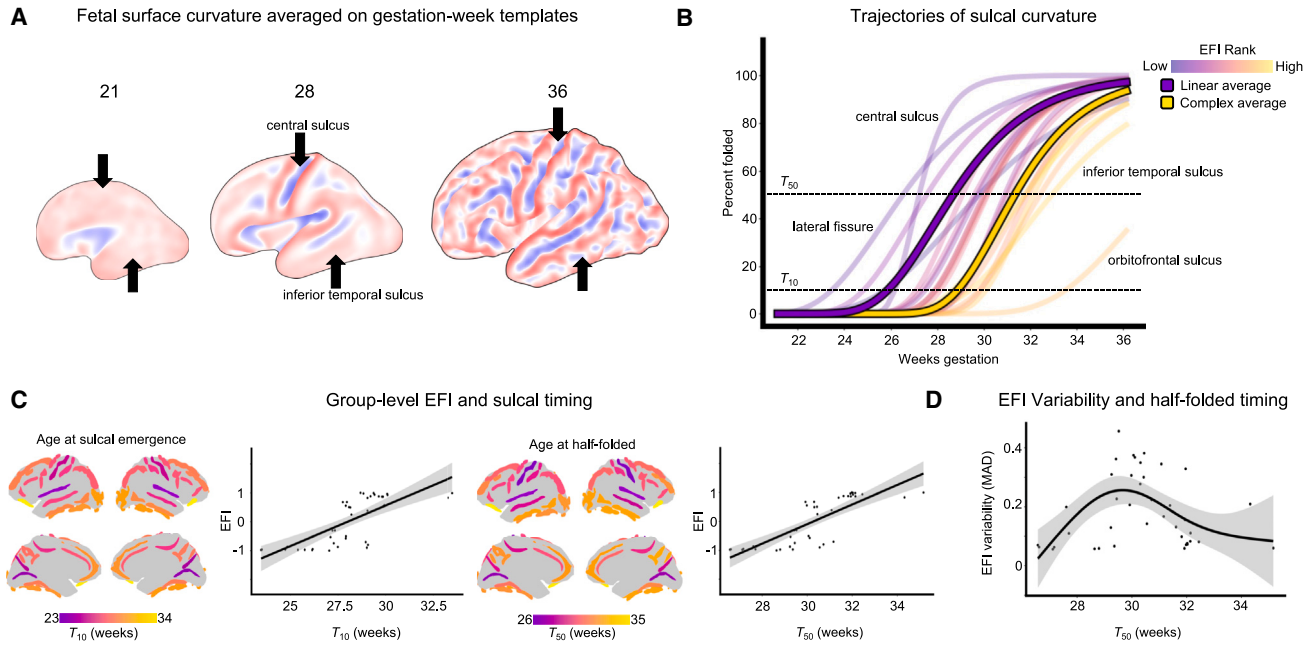

Figure 6. Trajectories of sulcal development in fetal brains are related to categorical (SPN modular) and dimensional (EFI) measures of adult sulcal patterning

(A) Exemplar cortical surface representations of the human fetal brain, as it develops, folds from gestational weeks 21–36, with exemplar linear (central sulcus) and complex sulci (inferior temporal sulcus) highlighted. Color codes bilaterally averaged sulcal curvature with negative (convex) curvature in red and positive (concave) curvature in blue.

(B) Trajectories of mean sulcal curvature as a function of GA were expressed as a percentage of the maximum or final curvature of each sulcus. Bilaterally averaged trajectories are shown for visualization purposes, but hemisphere-specific trajectories were resolved and used in subsequent analyses. Individual sulci were colored in a semi-transparent scale by their EFI ranking, with linear and complex sulcal cluster averages overlayed in solid colors. A sulcus was considered to have emerged once it reached 10% of maximal folding (T_{10}), at which point approximately the sulcal indentation is first visible to the human eye, and a sulcus was designated as half-folded at 50% of maximal curvature (T_{50}). Linear sulci (with EFI close to −1) fold on average earlier than complex sulci (with EFI close to +1), but there is large variation in sulcation timing within both linear and complex clusters.

(C) Gestational age at T_{10} and T_{50} was strongly correlated with sulcal differences with adult average EFI (T_{10}: $r = 0.73$, $p = 7.92 * 10^{-8}$; T_{50}: $r = 0.81$, $p = 3.43 * 10^{-10}$), indicating that more complexly branching sulci form later in development. The association is slightly stronger with T_{50}, near when folds undergo highest rates of regional expansion. In subsequent analyses, we focused on the GA at half-folded.

(D) Individual differences in sulcal EFI are related to T_{50}, with the earliest and latest folding sulci demonstrating much less between-subject variability in adult EFI than sulci folding at intermediate GAs ($p = 0.0015$). Lower individual variability in EFI of the first and last developing sulci presumably represents higher genetic or geometric constraints on their shape complexity.

See also Table S1 and Videos S1 and S2.

the higher loadings of areas adjacent to complex sulci, typical of heteromodal cortex.

Taken together, these categorical and dimensional analyses of adult sulcal patterning reveal a bimodal axis from linear to complex morphology. The distinct ordering of sulci along this shape axis not only coheres with other structural and functional measures but also demonstrates constraints at the most linear and complex poles, suggesting potentially different modes or phases of linear and complex sulcal development *in utero*.

Fetal sulcal emergence is linked to adult sulcal patterning

Based on these results and prior work,[2,3] we hypothesized that the linear-to-complex dimension of adult sulcal patterning could be rooted in the phased emergence of cortical sulci during fetal brain development. We directly tested this hypothesis by using brain MRI scans *in utero* for $n = 228$ fetuses aged 21–36 weeks GA (Figure 6A) to precisely quantify sulcus-specific trajectories or growth curves. Mapping against the prospective sulcal regions observed in adults (STAR Methods) allowed us to compare key milestones in when sulci form to how sulci present their shape in adulthood.

By tracking mean sulcal curvature over fetal life with a Gompertz growth model,[46] we captured development from 0% folding (lissencephaly, at 21 weeks GA) to 100% folded (relative plateau of curvature development, at 36 weeks GA) for each sulcus. Model fits were strong (R-squared > 80% for 95% of sulci) and were visualized with animations to confirm they matched the visual evolution of cortical folding along spatially interpolated fetal cortical surface templates (Videos S1 and S2). From these curves, we estimated key milestones in development of each sulcus, including the time to reach 10% maximum curvature, T_{10}, and the time to reach 50% maximum curvature, or half-folded, T_{50} (Figure 6B; Table S1). We found that both milestones of fetal sulcation were strongly positively correlated with EFI scores of the corresponding sulci in the adult brain

(T_{10}: r = 0.73, $p = 7.92 * 10^{-8}$; T_{50}: r = 0.81, $p = 3.43 * 10^{-10}$) (Figure 6C). In other words, sulci that had later sulcation milestones had more positive EFI scores, indicating more complex adult patterning. Convergently, sulcation milestones were significantly different between linear and complex clusters of the group mean SPN in terms of T_{10} (linear cluster mean = 26.6 weeks GA, complex cluster mean = 29.4 weeks GA; $t = -5.4$, $p < 0.05$) and T_{50} (linear cluster mean = 28.9, complex cluster mean = 31.7; $t = -6.5$, $p < 0.05$). The inter-subject variability of adult sulcal morphology, quantified by the MAD of sulcal EFI scores, had a significant non-linear relationship with sulcation milestones ($p = 0.0015$), as expected from prior results (Figure 4B). Sulci with earliest or latest milestones of emergence had much less inter-subject variability than sulci that emerged midway through the neurodevelopmental cascade of sulco-gyral patterning (Figure 6D). Thus, we found that differential timing of fetal sulcation across the cortex was strongly associated with the typical form and individual differences of each sulcus on the linear-to-complex dimension of adult sulcal patterning.

Assessment of gene expression differences across sulcal boundaries

It has previously been theorized that fetal sulcation could be driven by "buckling" of the cortical sheet at the boundaries between early-established zones of cytoarchitectonic differentiation between nascent cortical areas.[10,47–49] This model would predict that (1) sharper transitions from low to high gene expression, i.e., greater magnitude of tangential gradients of gene expression, are expected around the more genetically constrained linear sulci than complex sulci; and (2) genes with expression gradients that are strongly orthogonal to the fundus of linear folds in adulthood should proxy early-established cytoarchitectonic differences between neighboring cortical regions. We directly tested these mechanistic predictions by aligning the sulcal maps from our automated morphometry pipeline (STAR Methods) with spatially fine-grained cortical maps of tangential expression changes for 20,781 genes from Wagstyl et al.[50]

Confirming our first prediction, we found that the mean transcriptional gradient across all analyzed genes was indeed relatively increased in regions adjacent to bilaterally linear sulci, compared with regions adjacent to bilaterally complex sulci ($p_{spin} = 0.0152$) (Figure 7B). By focusing on the principal angle and magnitude of tangential gene expression changes in the vicinity of linear sulci (STAR Methods), we found that the central sulcus and parieto-occipital fissure in particular had pronounced trans-sulcal gradients of gene expression change aligned orthogonally to the fundus of each sulcus ($p_{spin} < 0.05$) (Figure 7C).

To test our second prediction, we characterized the genes that had significant trans-sulcal gradients of expression across each of 9 linear sulci (Figure 7D; Table S4). These gene rankings were most highly correlated between proximal or parallel sulci but were more weakly correlated between anatomically distant sulci (Figure 7E), suggesting that linear sulcation is underpinned by different trans-sulcal gradients of expression in different cortical regions.[51] Gene ontology enrichment analysis of trans-sulcal expression gradients for the central sulcus and parieto-occipital fissure highlighted multiple developmentally salient gene sets ($p_{spin} < 0.05$, Bonferroni corrected, Figure 7F; Table S5). For example, gene expression gradients orthogonal to the central sulcus were enriched for inhibitory neurons, microglia, oligodendrocyte precursor cells, cytoskeleton compartment, nuclear compartment, endosome compartment, and rare risk genes for autism spectrum disorder, schizophrenia, severe developmental disorders, and epilepsy. Each of these gradients represented a transition from low expression in pre-central gyrus to higher expression in post-central gyrus. The trans-sulcal gradient for the parieto-occipital fissure was distinctively enriched for layer V marker genes with expression generally increasing superior to the fissure in medial parietal cortex.

Additionally, since adult and fetal cell marker genes for cytoarchitecture share patterning in dense expression maps (DEMs),[50] we further tested for enrichment of fetal cell types. Fetal cell enrichments for the central sulcus were oriented along the same pre- to- post-central gyrus direction and included excitatory neurons (ExDp1/ExM-U), inhibitory migrating neurons (InMGE/InCGE), intermediate and cyclic progenitor cells (PgG2M/PgS), and fetal and perinatal gene sets ($p_{spin} < 0.05$, Bonferroni corrected). To provide further developmental context, we used measures of cortical gene expression between ~10 weeks GA and 40 years[52] to estimate developmental trajectories of expression for genes with tangential gradients of expression that were orthogonal to folds in the adult cortex. This procedure revealed that genes with significant trans-sulcal gradients across the central sulcus had peak cortex-wide expression during fetal development (Figures 7G and S6). Taken together, these findings supported our second hypothetical prediction that linear sulci in the adult brain are orientated such that they intersect or bisect large zones of rapid tangential change in gene expression.

DISCUSSION

We applied innovative tools for sulcal morphometry to large-scale MRI datasets on adult and fetal human brain structure to discover a bimodal organizational axis of SPNs linked to sulcal emergence *in utero*. By comparing against cortical measures from diverse datasets, we provide a deep annotation of this new perspective on human cortical surface patterning. We release this annotation along with containerized tools for automated sulcal morphometry and SPN analysis to accelerate future research on cortical folding. We consider each of the main outputs of our work in more detail below.

A new taxonomy of adult sulcal morphology

High-throughput sulcal morphometry in the UK Biobank cohort provided a unique dataset for quantitative analysis of human sulcal variation. Our approach integrated complementary diverse metrics of sulcal shape traditionally considered in isolation from each other. For example, sulcal depth has been related to cognition and developmental disorder.[3,13,19,20,36] Depth variability[39] captures sulcal pits and plis de passage (respectively, local maxima and minima of depth along the sulcal fundus), which are genetically constrained and functionally important features of sulcal anatomy.[53,54] Multiple studies have examined sulcal length in relation to developmental disorders and

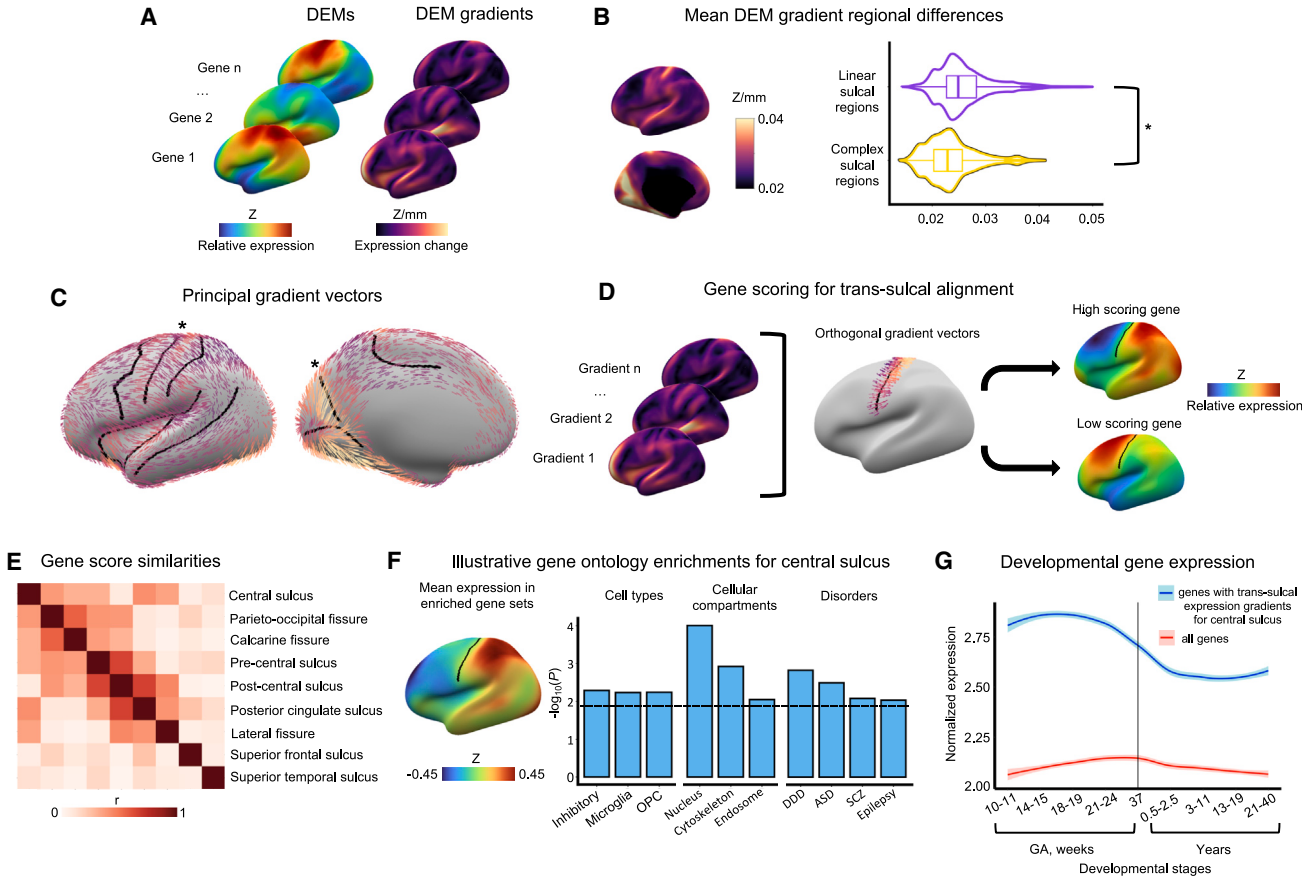

Figure 7. Developmentally salient cortical gene expression gradients are delineated by archetypal linear sulci

(A) Dense expression maps (DEMs) and their associated gradients were collated for 20,781 genes.

(B) Linear sulci had increased average DEM gradient compared with complex sulcal regions, indicating linear sulci were more likely to have signatures of tangential expression change (p_{spin} = 0.0152).

(C) The principal gene expression vectors, or dominant directions of gene expression change, significantly aligned with the central sulcus and parieto-occipital fissure ($p_{spin} < 0.05$).

(D) Sulcal fundi and gene expression were mapped to a common space from which gradient vectors and fundus orientation vectors were computed. Gene scores were given by the strength of the gradient and orthogonality (angle sine) of gradient and fundus vectors, with extreme low or high scores representing strong expression changes orthogonal either direction through the sulcal fundus (e.g., pre-post or post-pre central gyrus).

(E) {1 × 20,781} vectors of gene scores per linear sulcus were correlated, with absolute values of correlations higher between proximal or parallel sulci and lower between anatomically distant sulci.

(F) Exemplar gene ontology enrichments for gene scores are shown, with all central sulcus enrichments showing transitioning from low to high expression about pre- to post-central sulcus. The dashed line indicates the significance threshold, and displayed p values are capped at p = 1/10,000.

(G) Genes with significant trans-sulcal gradients across the adult central sulcus were mapped to the BrainSpan developmental brain gene expression dataset, revealing that these genes were enriched for expression during fetal life.

See also Figure S6 and Tables S4 and S5.

genetics.[17,18,20,40] Auzias et al.[55] found that the sulci with the longest branches were sufficiently consistent in their orientation (i.e., low branch span) to define latitudinal and longitudinal axes of the cortex. Only a few other studies have explicitly considered fractal geometry of brain gyrification[56] or sulcal shape, including studies of the FD of sulcal surfaces embedded in a 3D volume.[35,37] Here we used different but related fractal measures, focused on the embedding of sulcal lines tangent to the cortex, as innovative measures of sulcal non-linearity or complexity (Figure 1).

Leveraging this diverse set of sulcal shape phenotypes, we revealed two archetypes of sulcal organization, conver-

gently represented by distinct clusters of the SPN and by the bimodal distribution of sulci on a linear-to-complex dimension (EFI). Linear polar sulci, e.g., central sulcus and parieto-occipital fissure, were typically deep, straight (FD ∼ 1) indentations across unimodal cortex and were more heritable than complex polar sulci, e.g., orbito-frontal sulcus, which were typically shallow, complex (FD > 1), and located in heteromodal cortex. This bimodal taxonomy of sulcal patterning cohered with diverse other axes of cortical organization, including allometric scaling, gray matter thickness, and sensorimotor-association functional hierarchy[57] (Figure 5).

Timing of fetal formation of sulci was linked to polarity of adult sulcal shape

The clear bipartite clustering of the group mean SPN (Figure 3B) aligned approximately with prior postmortem measurements of fetal sulcal formation. To more comprehensively compare between dimensional measures of adult sulcal shape and fetal sulcation, we reconstructed cortical surfaces for 228 fetal brain MRI scans and estimated high temporal resolution trajectories of curvature development for each of 40 sulci identifiable in adult brains.

We confirmed that linear sulci (with EFI ~ -1) formed earlier than complex sulci (with EFI $\sim +1$), e.g., there was a strongly positive correlation between-adult sulcal EFI and the GA at which that sulcus was 50% (or 10%) fully formed *in utero* (Figure 6). Slightly stronger correlation was found with the 50% (T_{50}) milestone (r = 0.81), possibly because this milestone marks the peak rate of sulcal curvature development, likely co-occurring with rapid neurodevelopmental programs of tangential expansion of the cortical plate.[58] We also confirmed prior expectations that between-subject variability or individual uniqueness of adult sulcal shape should be minimized for linear sulci that formed earliest.[7,59]

Knowing that the earliest-forming, most linear sulci are more heritable, it is intuitive that their development should be stereotypically determined by a genetic program that is expressed regardless of stochastic or environmental differences between individual brains. However, more counter-intuitively, we also observed low levels of between-subject variability of adult shape for the most complex, latest-forming sulci (Figure 4), i.e., there was a non-linear, inverted-U relationship between individual variability of sulcal EFI and the milestone of 50% complete fetal sulcation (Figure 6). The most individually variable sulci had intermediate, less polarized values of EFI on average; emerged at intermediate GAs between the earliest, linear, and latest, complex sulci; and were sometimes directly proximal to sulci with the lowest between-subject variability of EFI (Figure 4). This variability could reflect competing mechanisms of cortical arealization driven by proximity to primary or unimodal cortex[60] met with stochastic buckling pressures midway through sulcal ontogenesis.

These observations suggest that fetal sulcation is more constrained (less individually different) at the start and the end than in the middle of the cascade of cortical folding. But the nature of such constraints remains to be parsed. Some studies frame sulcal development as a homogeneous process wherein all sulci form by the same mechanisms,[10] but recent models have begun to shed light on mechanistic heterogeneity between different sulci.[58] As noted, genetic constraints could explain the reduced sulcal complexity variability for the first-forming sulci. However, their relatively low heritability suggests that non-genetic constraints must apply to the latest forming, complex sulci. Just as models of crumpled paper demonstrate how further crumpling is constrained to maximally relieve tension in material,[61] the final cortical folds to form *in utero* could experience physical constraints on their formation due to multiple prior sulci having already "carved up" the cortical sheet available for new sulcation. The prior presence of sulci very likely impacts the later formation of proximal sulci,[47,62] so it is important for future studies to resolve more precisely how the end-point of the fetal sulcation cascade could be physically constrained.

Trans-sulcal expression gradients as a mechanism for linear sulcation

One prominent mechanistic model for sulcation is that the cortical sheet buckles under the physical stress of differential tangential expansion (DTE) between the stiffer cortical plate relative to deeper fetal tissue compartments.[58] Elaborations of the DTE model have considered that predictable location of sulcal in-folding could arise from differential expansion properties or cytoarchitecture of regions across the cortex.[62,63] Compatible with this model, linear sulci like the central sulcus and parieto-occipital fissure have long been recognized to demarcate cytoarchitectonically distinct areas,[48] with more recent histological work[49] demonstrating that primary fissures (comprising linear sulci) better predict cytoarchitectonic boundaries than sulci in association cortex (comprising of complex sulci). By this account, the topographical patterning of cortical gene expression that controls areal differentiation should relate to linear sulcal anatomy, with differential gene expression either side of the sulcal line or fundus being compatible with differential expansion of the adjacent cortical areas divided by the fundus.

To test this model, we used DEMs of cortical gene transcription that allowed us to measure the magnitude and geometric alignment of tangential expression gradients with specific sulcal fundi. First, as predicted hypothetically and by prior work,[48,49] we found that the magnitude of tangential gene expression gradients was indeed significantly greater in cortical regions adjacent to linear sulci than in regions adjacent to complex sulci. Second, we focused on a more detailed analysis of the angle as well as the magnitude of gene expression gradients with respect to 9 linear sulci, including the central sulcus and the parieto-occipital fissure. We reasoned that gene expression gradients driving sulcus formation by differentiation of adjacent cortical areas should be orientated orthogonal to the sulcal fundus. We identified genes with trans-sulcal expression gradients for linear sulci, with some consistency between physically proximal sulci but also clear evidence that different sulci were associated with genetically and functionally distinct trans-sulcal expression gradients. For example, trans-sulcal gradients across the central sulcus were enriched for genes associated with neuronal development and neurodevelopmental disorders, whereas the genes that were most differentially expressed across the parieto-occipital fissure were enriched for layer V neurons of medial parietal cortex.

These coordinated configurations of folding and gene expression in adulthood are consistent with a biophysical model where early-established cytoarchitectural gradients predispose the buckling cortical sheet to form sulci in stereotyped locations. It is also possible—although less likely—that the stereotyped location of linear sulci is aligned with but not caused by cytoarchitectonic differences, or is itself a mechanism by which cytoarchitectonic differences are achieved between neighboring cortical regions,[10,64] requiring further investigation. Genome-wide association study (GWAS) would be useful to further assess mechanisms for linear or complex sulcal formation; one prediction is that common variation in the cytoarchitectural genes we

identified would predict the shape of generally linear sulci or that complex sulci are regulated by genes important for cortical expansion. Previous work[17,18] suggests such an approach would require careful handling of shared brain volume effects and careful consideration of quality control impacts on GWAS estimates to disentangle potential regionally specific mechanisms for sulcal complexity expression.

Tools for high-throughput sulcal morphometry and SPN analysis

To facilitate future investigations, we provide our suite of new metrics for comprehensive characterization of sulcal morphology, which drove our main discovery of a bimodal taxonomy of sulcal morphology. Our sulcal morphometrics differ from previous works as they are designed to maximally differentiate sulci by region of cortex, reflecting inter-regional differences initiated *in utero* that track through the life span. This new containerized tool for SPN analysis is built on the foundation of the BrainVISA software but also represents a significant advance in technical capability for automated analysis of whole brain sulcal patterning from human MRI. Our containerized pipeline automatically generates the 5 new morphological metrics of average sulcal depth, depth variability, longest branch, branch span, and FD, in addition to subject-level SPN and EFI results. The pipeline can run from a single command within ~2 min for each MRI scan processed with BrainVISA Morphologist, or ~25 min from frequently generated FreeSurfer outputs, e.g., on a single CPU, 8 GB RAM, Linux machine.

Limitations and future considerations

There are several limitations inherent to the study's datasets and approaches. First, it will be important to apply our adult sulcal morphometry analyses to younger and more diverse cohorts to test the generalizability of this bimodal taxonomy of sulcal patterning and its links to fetal sulcation. Future studies should also consider novel sulcal segmentation procedures that do not rely on existing sulcal atlases, which are currently necessary to consistently measure sulci across subjects. Additionally, while we used the largest fetal brain imaging cohort available, questions remain regarding between-subject variability in sulcal emergence and in sulcal complexity that would only be accessible in a longitudinally scanned cohort followed up through term birth.

Overall, more work needs to be done to evaluate mechanisms of cellular differentiation and differential gene expression across linear and complex sulci. Popular model organisms for gyrencephalic development, like the ferret,[65] only have linear sulci, which could impede translational studies of the bimodal sulcal taxonomy evident in humans. We used adult human brain transcriptomics to infer cytoarchitectural patterns likely established by term birth since, to date, there are no human datasets of fetal gene expression encompassing the full 21–36 weeks GA period over which both linear and complex sulci form. While there are multiple resources for fine-grained single-cell spatiotemporal fetal brain transcriptomics,[66,67] no such resource covers both linear and complex sulcal regions with comparable sampling between regions for inclusion of sulcal banks or gyral peaks, unlike the adult transcriptional atlas. There are extant fetal gene expression data for the ~23 week GA period,[52] but they do not have sufficiently fine-grained spatial resolution to measure gene expression gradients as precisely as in DEMs of the adult brain. It is therefore a limitation that we have not been able to link fetal sulcation with the concurrent spatiotemporal emergence of trans-sulcal gene expression gradients.

Conclusion

We have introduced and applied new methods for measuring SPNs from human brain MRI. We have presented evidence in support of a bimodal taxonomy for adult sulcal shape that is directly linked to fetal development and in support of the more mechanistic hypothesis that linear sulcation is driven by trans-sulcal gradients of gene expression. The annotated datasets and computational tools used to generate these results are published as an open resource to facilitate future mechanistic, developmental, and clinical studies of sulcal patterning.

STAR★METHODS

Detailed methods are provided in the online version of this paper and include the following:

- KEY RESOURCES TABLE
- RESOURCE AVAILABILITY
  - Lead contact
  - Materials availability
  - Data and code availability
- METHOD DETAILS
  - UK Biobank cohort
  - Extraction of sulci and quality control
  - Sulcal phenotype networks (SPNs)
  - Categorical and dimensional analyses of SPNs
  - Test-retest reliability of sulcal measures
  - Structural and functional brain map annotation against SPNs
  - Fetal cortical surface processing
  - Transcriptional annotation of SPNs
- QUANTIFICATION AND STATISTICAL ANALYSIS

SUPPLEMENTAL INFORMATION

Supplemental information can be found online at https://doi.org/10.1016/j.neuron.2024.07.023.

ACKNOWLEDGMENTS

W.E.S. is a PhD student/candidate in the NIH Oxford-Cambridge Scholars Program and is also supported by the Gates-Cambridge Scholarship. W.E.S. and A.R. are supported by the Intramural Research Program of the National Institute of Mental Health (NIH annual report number ZIAMH002949). This work received computational support from the NIH HPC Biowulf cluster (http://hpc.nih.gov) and from the National Institute of Health Research (NIHR) Cambridge Biomedical Research Centre (mental health theme). P.E.V. is a fellow of MQ: Transforming Mental Health (MQF17_24). K.W. is supported by the Welcome Trust (215901/Z/19/Z). L.Z.J.W. is supported by the Commonwealth Scholarship Commission, United Kingdom. D.M. and A.G.T. are supported by the Intramural Research Program of the National Institute of Mental Health (NIH Annual Report number ZICMH002960). J.-F.M. is supported by the French Agence Nationale de la Recherche through the grants ANR-19-CE45-0022-01IFOPASUBA and ANR-20-CHIA-0027-01FOLDDICO. V.K. is supported by the MRC translation support award (MR/V036874/1) and the dHCP. We are grateful for the teams involved in the dHCP toward the collection and processing of fetal neuroimaging data. The dHCP is funded by the European Research Council under the European Union's Seventh

Framework Programme (FP/2007-2013)/ERC Grant Agreement no. 319456. We are thankful for the families that generously participated in the dHCP and UK Biobank studies. The UK Biobank data was obtained under application number 22875.

AUTHOR CONTRIBUTIONS

Conceptualization and methodology, W.E.S., P.E.V., A.R., and E.T.B.; data curation, W.E.S., V.K., K.W., L.Z.J.W., D.M., A.G.T., V.R.K., J.S., and E.C.R.; software implementation, W.E.S. and D.R.; formal analysis, W.E.S.; writing – original draft, W.E.S., A.R., and E.T.B.; writing – review and editing, W.E.S., P.E.V., V.K., K.W., L.Z.J.W., D.M., A.G.T., V.R.K., J.S., D.R., E.C.R., J.-F.M., A.R., and E.T.B.

DECLARATION OF INTERESTS

E.T.B. has consulted for Novartis, GlaxoSmithKline, SR One, Sosei Heptares, Boehringer Ingelheim, and Monument Therapeutics. E.T.B. and J.S. are co-founders and stockholders of Centile Bio Inc.

Received: November 18, 2023
Revised: May 22, 2024
Accepted: July 29, 2024
Published: August 22, 2024

REFERENCES

1. Silbereis, J.C., Pochareddy, S., Zhu, Y., Li, M., and Sestan, N. (2016). The cellular and molecular landscapes of the developing human central nervous system. Neuron *89*, 248–268. https://doi.org/10.1016/j.neuron.2015.12.008.
2. de Vareilles, H., Rivière, D., Mangin, J.F., and Dubois, J. (2023). Development of cortical folds in the human brain: an attempt to review biological hypotheses, early neuroimaging investigations and functional correlates. Dev. Cogn. Neurosci. *61*, 101249. https://doi.org/10.1016/j.dcn.2023.101249.
3. Chi, J.G., Dooling, E.C., and Gilles, F.H. (1977). Gyral development of the human brain. Ann. Neurol. *1*, 86–93. https://doi.org/10.1002/ana.410010109.
4. Armstrong, E., Schleicher, A., Omran, H., Curtis, M., and Zilles, K. (1995). The ontogeny of human gyrification. Cereb. Cortex *5*, 56–63. https://doi.org/10.1093/cercor/5.1.56.
5. Nishikuni, K., and Ribas, G.C. (2013). Study of fetal and postnatal morphological development of the brain sulci. J. Neurosurg. Pediatr. *11*, 1–11. https://doi.org/10.3171/2012.9.PEDS12122.
6. Cachia, A., Borst, G., Tissier, C., Fisher, C., Plaze, M., Gay, O., Rivière, D., Gogtay, N., Giedd, J., Mangin, J.F., et al. (2016). Longitudinal stability of the folding pattern of the anterior cingulate cortex during development. Dev. Cogn. Neurosci. *19*, 122–127. https://doi.org/10.1016/j.dcn.2016.02.011.
7. Cachia, A., Borst, G., Jardri, R., Raznahan, A., Murray, G.K., Mangin, J.-F., and Plaze, M. (2021). Towards deciphering the fetal foundation of normal cognition and cognitive symptoms from sulcation of the cortex. Front. Neuroanat. *15*, 712862. https://doi.org/10.3389/fnana.2021.712862.
8. Dubois, J., Lefèvre, J., Angleys, H., Leroy, F., Fischer, C., Lebenberg, J., Dehaene-Lambertz, G., Borradori-Tolsa, C., Lazeyras, F., Hertz-Pannier, L., et al. (2019). The dynamics of cortical folding waves and prematurity-related deviations revealed by spatial and spectral analysis of gyrification. NeuroImage *185*, 934–946. https://doi.org/10.1016/j.neuroimage.2018.03.005.
9. Babler, W.J. (1991). Embryologic development of epidermal ridges and their configurations. Birth Defects Orig. Artic. Ser. *27*, 95–112.
10. Llinares-Benadero, C., and Borrell, V. (2019). Deconstructing cortical folding: genetic, cellular and mechanical determinants. Nat. Rev. Neurosci. *20*, 161–176. https://doi.org/10.1038/s41583-018-0112-2.
11. Miller, J.A., and Weiner, K.S. (2022). Unfolding the evolution of human cognition. Trends Cogn. Sci. *26*, 735–737. https://doi.org/10.1016/j.tics.2022.06.008.
12. Heuer, K., Gulban, O.F., Bazin, P.-L., Osoianu, A., Valabregue, R., Santin, M., Herbin, M., and Toro, R. (2019). Evolution of neocortical folding: A phylogenetic comparative analysis of MRI from 34 primate species. Cortex J. Devoted Study Nerv. Syst. Behav. *118*, 275–291. https://doi.org/10.1016/j.cortex.2019.04.011.
13. Voorhies, W.I., Miller, J.A., Yao, J.K., Bunge, S.A., and Weiner, K.S. (2021). Cognitive insights from tertiary sulci in prefrontal cortex. Nat. Commun. *12*, 5122. https://doi.org/10.1038/s41467-021-25162-w.
14. Mangin, J.F., Rivière, D., Cachia, A., Duchesnay, E., Cointepas, Y., Papadopoulos-Orfanos, D., Collins, D.L., Evans, A.C., and Régis, J. (2004). Object-based morphometry of the cerebral cortex. IEEE Trans. Med. Imaging *23*, 968–982. https://doi.org/10.1109/TMI.2004.831204.
15. Mangin, J.F., Rivière, D., Cachia, A., Duchesnay, E., Cointepas, Y., Papadopoulos-Orfanos, D., Scifo, P., Ochiai, T., Brunelle, F., and Régis, J. (2004). A framework to study the cortical folding patterns. NeuroImage *23*, S129–S138. https://doi.org/10.1016/j.neuroimage.2004.07.019.
16. Borne, L., Rivière, D., Mancip, M., and Mangin, J.-F. (2020). Automatic labeling of cortical sulci using patch- or CNN-based segmentation techniques combined with bottom-up geometric constraints. Med. Image Anal. *62*, 101651. https://doi.org/10.1016/j.media.2020.101651.
17. Pizzagalli, F., Auzias, G., Yang, Q., Mathias, S.R., Faskowitz, J., Boyd, J.D., Amini, A., Rivière, D., McMahon, K.L., de Zubicaray, G.I., et al. (2020). The reliability and heritability of cortical folds and their genetic correlations across hemispheres. Commun. Biol. *3*, 510. https://doi.org/10.1038/s42003-020-01163-1.
18. Sun, B.B., Loomis, S.J., Pizzagalli, F., Shatokhina, N., Painter, J.N., Foley, C.N., Biogen Biobank Team, Jensen, M.E., McLaren, D.G., Chintapalli, S.S., et al. (2022). Genetic map of regional sulcal morphology in the human brain from UK Biobank data. Nat. Commun. *13*, 6071. https://doi.org/10.1038/s41467-022-33829-1.
19. Yao, J.K., Voorhies, W.I., Miller, J.A., Bunge, S.A., and Weiner, K.S. (2023). Sulcal depth in prefrontal cortex: a novel predictor of working memory performance. Cereb. Cortex *33*, 1799–1813. https://doi.org/10.1093/cercor/bhac173.
20. Auzias, G., Viellard, M., Takerkart, S., Villeneuve, N., Poinso, F., Fonséca, D.D., Girard, N., and Deruelle, C. (2014). Atypical sulcal anatomy in young children with autism spectrum disorder. NeuroImage Clin. *4*, 593–603. https://doi.org/10.1016/j.nicl.2014.03.008.
21. White, T., and Hilgetag, C.C. (2011). Gyrification and neural connectivity in schizophrenia. Dev. Psychopathol. *23*, 339–352. https://doi.org/10.1017/S0954579410000842.
22. Gregory, M.D., Kippenhan, J.S., Dickinson, D., Carrasco, J., Mattay, V.S., Weinberger, D.R., and Berman, K.F. (2016). Regional variations in brain gyrification are associated with general cognitive ability in humans. Curr. Biol. *26*, 1301–1305. https://doi.org/10.1016/j.cub.2016.03.021.
23. Sanfelici, R., Ruef, A., Antonucci, L.A., Penzel, N., Sotiras, A., Dong, M.S., Urquijo-Castro, M., Wenzel, J., Kambeitz-Ilankovic, L., Hettwer, M.D., et al. (2022). Novel gyrification networks reveal links with psychiatric risk factors in early illness. Cereb. Cortex *32*, 1625–1636. https://doi.org/10.1093/cercor/bhab288.
24. Alexander-Bloch, A.F., Raznahan, A., Vandekar, S.N., Seidlitz, J., Lu, Z., Mathias, S.R., Knowles, E., Mollon, J., Rodrigue, A., Curran, J.E., et al. (2020). Imaging local genetic influences on cortical folding. Proc. Natl. Acad. Sci. USA *117*, 7430–7436. https://doi.org/10.1073/pnas.1912064117.
25. Warrier, V., Stauffer, E.-M., Huang, Q.Q., Wigdor, E.M., Slob, E.A.W., Seidlitz, J., Ronan, L., Valk, S.L., Mallard, T.T., Grotzinger, A.D., et al. (2023). Genetic insights into human cortical organization and development through genome-wide analyses of 2,347 neuroimaging phenotypes. Nat. Genet. *55*, 1483–1493. https://doi.org/10.1038/s41588-023-01475-y.

26. Seidlitz, J., Váša, F., Shinn, M., Romero-Garcia, R., Whitaker, K.J., Vértes, P.E., Wagstyl, K., Kirkpatrick Reardon, P., Clasen, L., Liu, S., et al. (2018). Morphometric similarity networks detect microscale cortical organization and predict inter-individual cognitive variation. Neuron *97*, 231–247.e7. https://doi.org/10.1016/j.neuron.2017.11.039.

27. Miller, K.L., Alfaro-Almagro, F., Bangerter, N.K., Thomas, D.L., Yacoub, E., Xu, J., Bartsch, A.J., Jbabdi, S., Sotiropoulos, S.N., Andersson, J.L.R., et al. (2016). Multimodal population brain imaging in the UK Biobank prospective epidemiological study. Nat. Neurosci. *19*, 1523–1536. https://doi.org/10.1038/nn.4393.

28. Littlejohns, T.J., Holliday, J., Gibson, L.M., Garratt, S., Oesingmann, N., Alfaro-Almagro, F., Bell, J.D., Boultwood, C., Collins, R., Conroy, M.C., et al. (2020). The UK biobank imaging enhancement of 100,000 participants: rationale, data collection, management and future directions. Nat. Commun. *11*, 2624. https://doi.org/10.1038/s41467-020-15948-9.

29. Edwards, A.D., Rueckert, D., Smith, S.M., Abo Seada, S., Alansary, A., Almalbis, J., Allsop, J., Andersson, J., Arichi, T., Arulkumaran, S., et al. (2022). The developing human connectome project neonatal data release. Front. Neurosci. *16*, 886772. https://doi.org/10.3389/fnins.2022.886772.

30. Fischl, B., Salat, D.H., Busa, E., Albert, M., Dieterich, M., Haselgrove, C., van der Kouwe, A., Killiany, R., Kennedy, D., Klaveness, S., et al. (2002). Whole brain segmentation: automated labeling of neuroanatomical structures in the human brain. Neuron *33*, 341–355. https://doi.org/10.1016/s0896-6273(02)00569-x.

31. Fischl, B., van der Kouwe, A., Destrieux, C., Halgren, E., Ségonne, F., Salat, D.H., Busa, E., Seidman, L.J., Goldstein, J., Kennedy, D., et al. (2004). Automatically parcellating the human cerebral cortex. Cereb. Cortex *14*, 11–22. https://doi.org/10.1093/cercor/bhg087.

32. Cox, S.R., Ritchie, S.J., Fawns-Ritchie, C., Tucker-Drob, E.M., and Deary, I.J. (2019). Structural brain imaging correlates of general intelligence in UK Biobank. Intelligence *76*, 101376. https://doi.org/10.1016/j.intell.2019.101376.

33. Makropoulos, A., Robinson, E.C., Schuh, A., Wright, R., Fitzgibbon, S., Bozek, J., Counsell, S.J., Steinweg, J., Vecchiato, K., Passerat-Palmbach, J., et al. (2018). The developing human connectome project: A minimal processing pipeline for neonatal cortical surface reconstruction. NeuroImage *173*, 88–112. https://doi.org/10.1016/j.neuroimage.2018.01.054.

34. Ono, M., Kubik, S., and Abarnathey, C.D. (1990). Atlas of the Cerebral Sulci (Thieme Medical Publishers, Inc.).

35. Thompson, P.M., Schwartz, C., Lin, R.T., Khan, A.A., and Toga, A.W. (1996). Three-dimensional statistical analysis of sulcal variability in the human brain. J. Neurosci. *16*, 4261–4274. https://doi.org/10.1523/JNEUROSCI.16-13-04261.1996.

36. Régis, J., Mangin, J.-F., Ochiai, T., Frouin, V., Riviére, D., Cachia, A., Tamura, M., and Samson, Y. (2005). "Sulcal root" generic model: a hypothesis to overcome the variability of the human cortex folding patterns. Neurol. Med. Chir. (Tokyo) *45*, 1–17. https://doi.org/10.2176/nmc.45.1.

37. Li, S., Xia, M., Pu, F., Li, D., Fan, Y., Niu, H., Pei, B., and He, Y. (2011). Age-related changes in the surface morphology of the central sulcus. NeuroImage *58*, 381–390. https://doi.org/10.1016/j.neuroimage.2011.06.041.

38. Levy, M., Lu, Z., Dion, G., and Kara, P. (2014). The shape of dendritic arbors in different functional domains of the cortical orientation map. J. Neurosci. *34*, 3231–3236. https://doi.org/10.1523/JNEUROSCI.4985-13.2014.

39. Klein, A., Ghosh, S.S., Bao, F.S., Giard, J., Häme, Y., Stavsky, E., Lee, N., Rossa, B., Reuter, M., Chaibub Neto, E.C., et al. (2017). Mindboggling morphometry of human brains. PLOS Comput. Biol. *13*, e1005350. https://doi.org/10.1371/journal.pcbi.1005350.

40. Fish, A.M., Cachia, A., Fischer, C., Mankiw, C., Reardon, P.K., Clasen, L.S., Blumenthal, J.D., Greenstein, D., Giedd, J.N., Mangin, J.-F., et al. (2017). Influences of brain size, sex, and sex chromosome complement on the architecture of human cortical folding. Cereb. Cortex *27*, 5557–5567. https://doi.org/10.1093/cercor/bhw323.

41. Reardon, P.K., Seidlitz, J., Vandekar, S., Liu, S., Patel, R., Park, M.T.M., Alexander-Bloch, A., Clasen, L.S., Blumenthal, J.D., Lalonde, F.M., et al. (2018). Normative brain size variation and brain shape diversity in humans. Science *360*, 1222–1227. https://doi.org/10.1126/science.aar2578.

42. Gould, S.J. (1966). Allometry and size in ontogeny and phylogeny. Biol. Rev. Camb. Philos. Soc. *41*, 587–640. https://doi.org/10.1111/j.1469-185x.1966.tb01624.x.

43. Perrot, M., Rivière, D., and Mangin, J.-F. (2011). Cortical sulci recognition and spatial normalization. Med. Image Anal. *15*, 529–550. https://doi.org/10.1016/j.media.2011.02.008.

44. Yarkoni, T., Poldrack, R.A., Nichols, T.E., Van Essen, D.C., and Wager, T.D. (2011). Large-scale automated synthesis of human functional neuroimaging data. Nat. Methods *8*, 665–670. https://doi.org/10.1038/nmeth.1635.

45. Margulies, D.S., Ghosh, S.S., Goulas, A., Falkiewicz, M., Huntenburg, J.M., Langs, G., Bezgin, G., Eickhoff, S.B., Castellanos, F.X., Petrides, M., et al. (2016). Situating the default-mode network along a principal gradient of macroscale cortical organization. Proc. Natl. Acad. Sci. USA *113*, 12574–12579. https://doi.org/10.1073/pnas.1608282113.

46. Xu, X., Sun, C., Sun, J., Shi, W., Shen, Y., Zhao, R., Luo, W., Li, M., Wang, G., and Wu, D. (2022). Spatiotemporal atlas of the fetal brain depicts cortical developmental gradient. J. Neurosci. *42*, 9435–9449. https://doi.org/10.1523/JNEUROSCI.1285-22.2022.

47. Kroenke, C.D., and Bayly, P.V. (2018). How forces fold the cerebral cortex. J. Neurosci. *38*, 767–775. https://doi.org/10.1523/JNEUROSCI.1105-17.2017.

48. von Economo, and Koskinas. (1925). The Cytoarchitectonics of the Adult Human Cerebral Cortex (Springer).

49. Fischl, B., Rajendran, N., Busa, E., Augustinack, J., Hinds, O., Yeo, B.T.T., Mohlberg, H., Amunts, K., and Zilles, K. (2008). Cortical folding patterns and predicting cytoarchitecture. Cereb. Cortex *18*, 1973–1980. https://doi.org/10.1093/cercor/bhm225.

50. Wagstyl, K., Adler, S., Seidlitz, J., Vandekar, S., Mallard, T.T., Dear, R., DeCasien, A.R., Satterthwaite, T.D., Liu, S., Vértes, P.E., et al. (2024). Transcriptional cartography integrates multiscale biology of the human cortex. eLife *12*, RP86933. https://doi.org/10.7554/eLife.86933.

51. Vogel, J.W., Alexander-Bloch, A., Wagstyl, K., Bertolero, M., Markello, R., Pines, A., Sydnor, V.J., Diaz-Papkovich, A., Hansen, J., Evans, A.C., et al. (2022). Conserved whole-brain spatiomolecular gradients shape adult brain functional organization. Preprint at bioRxiv. https://doi.org/10.1101/2022.09.18.508425.

52. Miller, J.A., Ding, S.-L., Sunkin, S.M., Smith, K.A., Ng, L., Szafer, A., Ebbert, A., Riley, Z.L., Royall, J.J., Aiona, K., et al. (2014). Transcriptional landscape of the prenatal human brain. Nature *508*, 199–206. https://doi.org/10.1038/nature13185.

53. Im, K., and Grant, P.E. (2019). Sulcal pits and patterns in developing human brains. NeuroImage *185*, 881–890. https://doi.org/10.1016/j.neuroimage.2018.03.057.

54. Mangin, J.-F., Le Guen, Y., Labra, N., Grigis, A., Frouin, V., Guevara, M., Fischer, C., Rivière, D., Hopkins, W.D., Régis, J., et al. (2019). "Plis de passage" Deserve a Role in Models of the Cortical Folding Process. Brain Topogr. *32*, 1035–1048. https://doi.org/10.1007/s10548-019-00734-8.

55. Auzias, G., Lefèvre, J., Le Troter, A., Fischer, C., Perrot, M., Régis, J., and Coulon, O. (2013). Model-driven harmonic parameterization of the cortical surface: HIP-HOP. IEEE Trans. Med. Imaging *32*, 873–887. https://doi.org/10.1109/TMI.2013.2241651.

56. Bullmore, E., Brammer, M., Harvey, I., Persaud, R., Murray, R., and Ron, M. (1994). Fractal analysis of the boundary between white matter and cerebral cortex in magnetic resonance images: a controlled study of schizophrenic and manic-depressive patients. Psychol. Med. *24*, 771–781. https://doi.org/10.1017/s0033291700027926.

57. Sydnor, V.J., Larsen, B., Bassett, D.S., Alexander-Bloch, A., Fair, D.A., Liston, C., Mackey, A.P., Milham, M.P., Pines, A., Roalf, D.R., et al. (2021). Neurodevelopment of the association cortices: patterns, mechanisms, and implications for psychopathology. Neuron *109*, 2820–2846. https://doi.org/10.1016/j.neuron.2021.06.016.

58. Van Essen, D.C. (2020). A 2020 view of tension-based cortical morphogenesis. Proc. Natl. Acad. Sci. USA *117*, 32868–32879. https://doi.org/10.1073/pnas.2016830117.

59. Lohmann, G., von Cramon, D.Y., and Steinmetz, H. (1999). Sulcal variability of twins. Cereb. Cortex *9*, 754–763. https://doi.org/10.1093/cercor/9.7.754.

60. Buckner, R.L., and Krienen, F.M. (2013). The evolution of distributed association networks in the human brain. Trends Cogn. Sci. *17*, 648–665. https://doi.org/10.1016/j.tics.2013.09.017.

61. Andrejevic, J., Lee, L.M., Rubinstein, S.M., and Rycroft, C.H. (2021). A model for the fragmentation kinetics of crumpled thin sheets. Nat. Commun. *12*, 1470. https://doi.org/10.1038/s41467-021-21625-2.

62. Bayly, P.V., Okamoto, R.J., Xu, G., Shi, Y., and Taber, L.A. (2013). A cortical folding model incorporating stress-dependent growth explains gyral wavelengths and stress patterns in the developing brain. Phys. Biol. *10*, 016005. https://doi.org/10.1088/1478-3975/10/1/016005.

63. Garcia, K.E., Kroenke, C.D., and Bayly, P.V. (2018). Mechanics of cortical folding: stress, growth and stability. Philos. Trans. R. Soc. Lond. B Biol. Sci. *373*, 20170321. https://doi.org/10.1098/rstb.2017.0321.

64. Heuer, K., and Toro, R. (2019). Role of mechanical morphogenesis in the development and evolution of the neocortex. Phys. Life Rev. *31*, 233–239. https://doi.org/10.1016/j.plrev.2019.01.012.

65. de Juan Romero, C., Bruder, C., Tomasello, U., Sanz-Anquela, J.M., and Borrell, V. (2015). Discrete domains of gene expression in germinal layers distinguish the development of gyrencephaly. EMBO J. *34*, 1859–1874. https://doi.org/10.15252/embj.201591176.

66. Velmeshev, D., Perez, Y., Yan, Z., Valencia, J.E., Castaneda-Castellanos, D.R., Wang, L., Schirmer, L., Mayer, S., Wick, B., Wang, S., et al. (2023). Single-cell analysis of prenatal and postnatal human cortical development. Science *382*, eadf0834. https://doi.org/10.1126/science.adf0834.

67. Wang, L., Wang, C., Moriano, J.A., Chen, S., Zhang, S., Mukhtar, T., Wang, S., Cebrián-Silla, A., Bi, Q., Augustin, J.J., et al. (2024). Molecular and cellular dynamics of the developing human neocortex at single-cell resolution. Preprint at bioRxiv. https://doi.org/10.1101/2024.01.16.575956.

68. Landman, B.A., Huang, A.J., Gifford, A., Vikram, D.S., Lim, I.A.L., Farrell, J.A.D., Bogovic, J.A., Hua, J., Chen, M., Jarso, S., et al. (2011). Multi-parametric neuroimaging reproducibility: a 3-T resource study. NeuroImage *54*, 2854–2866. https://doi.org/10.1016/j.neuroimage.2010.11.047.

69. Poldrack, R.A., Mumford, J.A., Schonberg, T., Kalar, D., Barman, B., and Yarkoni, T. (2012). Discovering relations between mind, brain, and mental disorders using topic mapping. PLoS Comput. Biol. *8*, e1002707. https://doi.org/10.1371/journal.pcbi.1002707.

70. Markello, R.D., Hansen, J.Y., Liu, Z.-Q., Bazinet, V., Shafiei, G., Suárez, L.E., Blostein, N., Seidlitz, J., Baillet, S., Satterthwaite, T.D., et al. (2022). neuromaps: structural and functional interpretation of brain maps. Nat. Methods *19*, 1472–1479. https://doi.org/10.1038/s41592-022-01625-w.

71. Li, M., Santpere, G., Imamura Kawasawa, Y., Evgrafov, O.V., Gulden, F.O., Pochareddy, S., Sunkin, S.M., Li, Z., Shin, Y., Zhu, Y., et al. (2018). Integrative functional genomic analysis of human brain development and neuropsychiatric risks. Science *362*, eaat7615. https://doi.org/10.1126/science.aat7615.

72. Makropoulos, A., Gousias, I.S., Ledig, C., Aljabar, P., Serag, A., Hajnal, J.V., Edwards, A.D., Counsell, S.J., and Rueckert, D. (2014). Automatic whole brain MRI segmentation of the developing neonatal brain. IEEE Trans. Med. Imaging *33*, 1818–1831. https://doi.org/10.1109/TMI.2014.2322280.

73. Robinson, E.C., Jbabdi, S., Glasser, M.F., Andersson, J., Burgess, G.C., Harms, M.P., Smith, S.M., Van Essen, D.C., and Jenkinson, M. (2014). MSM: a new flexible framework for Multimodal Surface Matching☆. NeuroImage *100*, 414–426. https://doi.org/10.1016/j.neuroimage.2014.05.069.

74. Fernández-Pena, A., Martín de Blas, D., Navas-Sánchez, F.J., Marcos-Vidal, L., M Gordaliza, P., Santonja, J., Janssen, J., Carmona, S., Desco, M., and Alemán-Gómez, Y. (2023). ABLE: automated brain lines extraction based on laplacian surface collapse. Neuroinformatics *21*, 145–162. https://doi.org/10.1007/s12021-022-09601-7.

75. Marcus, D.S., Harwell, J., Olsen, T., Hodge, M., Glasser, M.F., Prior, F., Jenkinson, M., Laumann, T., Curtiss, S.W., and Van Essen, D.C. (2011). Informatics and data mining tools and strategies for the human connectome project. Front. Neuroinform. *5*, 4. https://doi.org/10.3389/fninf.2011.00004.

76. Stauffer, E.-M., Bethlehem, R.A.I., Dorfschmidt, L., Won, H., Warrier, V., and Bullmore, E.T. (2023). The genetic relationships between brain structure and schizophrenia. Nat. Commun. *14*, 7820. https://doi.org/10.1038/s41467-023-43567-7.

77. Alfaro-Almagro, F., Jenkinson, M., Bangerter, N.K., Andersson, J.L.R., Griffanti, L., Douaud, G., Sotiropoulos, S.N., Jbabdi, S., Hernandez-Fernandez, M., Vallee, E., et al. (2018). Image processing and Quality Control for the first 10,000 brain imaging datasets from UK Biobank. NeuroImage *166*, 400–424. https://doi.org/10.1016/j.neuroimage.2017.10.034.

78. Mallard, T.T., Liu, S., Seidlitz, J., Ma, Z., Moraczewski, D., Thomas, A., and Raznahan, A. (2021). X-chromosome influences on neuroanatomical variation in humans. Nat. Neurosci. *24*, 1216–1224. https://doi.org/10.1038/s41593-021-00890-w.

79. Esteban, O., Blair, R., Markiewicz, C.J., Berleant, S.L., Moodie, C., Ma, F., Isik, A.I., Erramuzpe, A., Goncalves, M., Poldrack, R.A., et al. (2017). poldracklab/fmriprep: 1.0.0-rc5, version 1.0.0-rc5 (Zenodo). https://doi.org/10.5281/zenodo.996169.

80. Rosen, A.F.G., Roalf, D.R., Ruparel, K., Blake, J., Seelaus, K., Villa, L.P., Ciric, R., Cook, P.A., Davatzikos, C., Elliott, M.A., et al. (2018). Quantitative assessment of structural image quality. NeuroImage *169*, 407–418. https://doi.org/10.1016/j.neuroimage.2017.12.059.

81. Bethlehem, R., Bethlehem, R.A.I., Seidlitz, J., White, S.R., Vogel, J.W., Anderson, K.M., Adamson, C., Adler, S., Alexopoulos, G.S., Anagnostou, E., Areces-Gonzalez, A., et al. (2022). Brain charts for the human lifespan. Nature *604*, 525–533. https://doi.org/10.1038/s41586-022-04554-y.

82. Destrieux, C., Fischl, B., Dale, A., and Halgren, E. (2010). Automatic parcellation of human cortical gyri and sulci using standard anatomical nomenclature. NeuroImage *53*, 1–15. https://doi.org/10.1016/j.neuroimage.2010.06.010.

83. Alexander-Bloch, A.F., Shou, H., Liu, S., Satterthwaite, T.D., Glahn, D.C., Shinohara, R.T., Vandekar, S.N., and Raznahan, A. (2018). On testing for spatial correspondence between maps of human brain structure and function. NeuroImage *178*, 540–551. https://doi.org/10.1016/j.neuroimage.2018.05.070.

84. Schuh, A., Makropoulos, A., Wright, R., Robinson, E.C., Tusor, N., Steinweg, J., Hughes, E., Cordero Grande, L., Price, A., Hutter, J., et al. (2017). A deformable model for the reconstruction of the neonatal cortex. In 2017 IEEE 14th International Symposium on Biomedical Imaging (ISBI 2017), pp. 800–803. https://doi.org/10.1109/ISBI.2017.7950639.

85. Karolis, V., Williams, L., Kyriakopoulou, V., Bozek, J., Uus, A., Makropoulos, A., Schuh, A., Cordero Grande, L., Hughes, E., Price, A., et al. (2023). Developing Human Connectome Project Spatio-temporal Surface Atlas of the Fetal Brain, version 1.0 ([object Object]). https://doi.org/10.12751/G-NODE.QJ5HS7.

86. Robinson, E.C., Garcia, K., Glasser, M.F., Chen, Z., Coalson, T.S., Makropoulos, A., Bozek, J., Wright, R., Schuh, A., Webster, M., et al. (2018). Multimodal surface matching with higher-order smoothness constraints. NeuroImage *167*, 453–465. https://doi.org/10.1016/j.neuroimage.2017.10.037.

87. Serag, A., Aljabar, P., Counsell, S., Boardman, J., Hajnal, J.V., and Rueckert, D. (2012). LISA: longitudinal image registration via spatio-temporal atlases. In 9th IEEE International Symposium on Biomedical Imaging (ISBI), pp. 334–337. https://doi.org/10.1109/ISBI.2012.6235552.

88. Oldham, S., Fulcher, B.D., Aquino, K., Arnatkevičiūtė, A., Paquola, C., Shishegar, R., and Fornito, A. (2022). Modeling spatial, developmental, physiological, and topological constraints on human brain connectivity. Sci. Adv. *8*, eabm6127. https://doi.org/10.1126/sciadv.abm6127.

89. Van Essen, D.C., and Drury, H.A. (1997). Structural and functional analyses of human cerebral cortex using a surface-based atlas. J. Neurosci. *17*, 7079–7102. https://doi.org/10.1523/JNEUROSCI.17-18-07079.1997.

90. Wood, S.N. (2011). Fast stable restricted maximum likelihood and marginal likelihood estimation of semiparametric generalized linear models. J. R. Stat. Soc. B *73*, 3–36. https://doi.org/10.1111/j.1467-9868.2010.00749.x.

91. Fulcher, B.D., Arnatkeviciute, A., and Fornito, A. (2021). Overcoming false-positive gene-category enrichment in the analysis of spatially resolved transcriptomic brain atlas data. Nat. Commun. *12*, 2669. https://doi.org/10.1038/s41467-021-22862-1.

STAR★METHODS

KEY RESOURCES TABLE

REAGENT or RESOURCE	SOURCE	IDENTIFIER
Deposited data		
Benchmark adult, fetal, and transcriptional sulcal annotations	This paper	Supplemental tables, GitHub: https://github.com/willsnyder12/sulcal_phenotype_networks
UK Biobank	Miller et al.[27]	https://www.ukbiobank.ac.uk
dHCP fetal MRI	Edwards et al.[29]	https://nda.nih.gov/edit_collection.html?id=3955
Multi-modal MRI reproducibility resource	Landmann et al.[68]	https://www.nitrc.org/projects/multimodal/
Neurosynth functional MRI topic maps	Poldrak et al.[69]	https://neurosynth.org/analyses/topics/v4-topics-50/
NeuroMaps	Markello et al.[70]	https://github.com/netneurolab/neuromaps
Dense cortical expression maps (DEMs)	Wagstyl et al.[50]	https://figshare.com/s/82c8f6ebda38af670cd1
PsychEncode processed BrainSpan data	Li et al.[71]	http://development.psychencode.org/
Software and algorithms		
Sulcal Phenotype Network container and analysis	This paper	SPN container, Figshare: https://doi.org/10.6084/m9.figshare.25874425 (DOI active prior to publication) Additional analysis code, GitHub: https://github.com/willsnyder12/sulcal_phenotype_networks
FreeSurfer	Fischl[30]	http://surfer.nmr.mgh.harvard.edu
BrainVISA Morphologist	Mangin et al.[14]	http://brainvisa.info
Smallest Enclosing circle	Project Nayuki	https://www.nayuki.io/page/smallest-enclosing-circle
3D Fractal dimension calculation	Chatzigeorgiou Lab	https://github.com/ChatzigeorgiouGroup/FractalDimension
R	R Development Core Team	https://www.r-project.org/
netneurotools	Network Neuroscience Lab	https://github.com/netneurolab/netneurotools
DRAW-EM	Makropoulos et al.[72]	https://github.com/MIRTK/DrawEM
MSM	Robinson et al.[73]	https://fsl.fmrib.ox.ac.uk/fsl/fslwiki/MSM
Python	Python Software Foundation	https://www.python.org/
ABLE	Fernández-Pena et al.[74]	https://github.com/HGGM-LIM/ABLE
MATLAB	MathWorks	https://www.mathworks.com/
Brain development animation	Stuart Oldham	https://github.com/StuartJO/BrainSurfaceAnimation
Connectome Workbench	Marcus et al.[75]	https://www.humanconnectome.org/software/get-connectome-workbench
Developmental gene expression analysis	Stauffer et al.[76]	https://github.com/evastauffer/schizophrenia-and-brain-structure

RESOURCE AVAILABILITY

Lead contact

Further information and requests for resources should be directed to and will be fulfilled by the lead contact, William Snyder (will.snyder@nih.gov).

Materials availability

This study did not generate new materials other than data and code.

Data and code availability

- Benchmark adult, fetal, and transcriptional sulcal annotation data are included in Supplemental Tables and have been deposited on GitHub. Website access to this data and publicly available source data used to derive it are listed in the key resources table.
- All original code for the sulcal phenotype networks pipeline and main analysis is deposited on GitHub and Figshare and is publicly available prior to the date of publication. We provide this code as a containerized pipeline (DOI active prior to publication) to derive sulcal phenotypes directly from brain scans processed by the frequently used FreeSurfer neuroimaging software. The GitHub website and DOI are listed in the key resources table.
- Any additional information required to reanalyze the data reported in this paper is available from the lead contact upon request.

METHOD DETAILS

UK Biobank cohort

The UK Biobank is an effort led to collect diverse phenotypic data to promote population-level assessments of lifestyle, environment, and genetics on biology and health presentation. A subset of subjects enrolled in the study participated in brain imaging, from which the first imaging session's data were retrieved (https://www.ukbiobank.ac.uk).[27,28]

Scanner acquisition of brain structural MRI is detailed elsewhere (https://biobank.ctsu.ox.ac.uk/crystal/crystal/docs/brain_mri.pdf). In brief, all three scanning sites used standard Siemens Skyra 3T scanners with a Siemens 32-channel RF receive head coil. T1 and T2-FLAIR acquisitions were both downloaded to support gray and white matter tissue segmentation. T1 acquisition involved a five-minute 3D MPRAGE session at 1x1x1 mm resolution, in-plane acceleration iPAT=2, and prescan-normalization. T2-FLAIR acquisition involved a six-minute 3D SPACE session at 1.05x1x1 mm resolution, in-plane acceleration iPAT=2, partial Fourier = 7/8, fat saturation, elliptical k-space scanning, and pre-scan normalization.[77]

Extraction of sulci and quality control

Cortical surfaces were first reconstructed for all subjects with T1 images and additionally with T2- FLAIR images if available as in Mallard et al.[78] using FreeSurfer neuroimaging software (version 6.0.1)[30,31] packaged in fmriprep 21.0.2.[79] FreeSurfer segmented boundaries of gray and white matter from the images, which were input to BrainVISA neuroimaging software (version compiled on August 8th, 2022) for watershed algorithm detection of sulcal boundaries. BrainVISA's Morphologist pipeline was used to extract sulci as the regions filling between gyral peaks, subsequently skeletonized to the wall of voxels halfway between bordering gyri.[14–16] All sulcal phenotypes were derived from points defined on the tops and bottoms of the voxel medial walls (Figure 1A, right).

After excluding $n = 1{,}568$ subjects with neurological conditions,[32] three quality control measures were implemented. First, previous work has demonstrated that robust automated quality control of MRI can be performed by detecting outliers of FreeSurfer mesh reconstruction quality.[80] As is standard,[81] outlier detection of Euler Number (EN) was performed within each scanning site, with interquartile range outliers excluded from analysis ($n = 2{,}026$). The second quality control procedure was to define a set of sulci measurable in virtually all subjects such that subjects without all labeled sulci were considered to have failed the BrainVISA Morphologist sulcal labeling pipeline. Previous works have excluded small sulci not labeled by BrainVISA in the majority of subjects.[17,18,20] We found that retaining 51 out of 123 possible bilateral sulcal labels allowed 95% of the original sample to be retained, with significant drop-off in the analyzable sample for any additional included sulci. From this set, we excluded sulci without anatomical meaning consistent with other sulci (i.e., the anterior lateral fissure label does not trace between gyri), included additional sulci that were components of larger sulcal regions, and then merged anatomically adjacent labels from a set of 64 sulcal labels (e.g., merging five labels of the pre-central sulcus into one label), mitigating BrainVISA Morphologist mislabeling that typically propagates between anatomically proximal regions (Figure S2). We retained labels for 20 sulci per hemisphere that spanned the lateral, medial, and ventral faces of the cortex (Figure S2) and were identifiable in almost all subjects. A small set of subjects that did not receive a label for one of these 40 major sulcal regions were excluded from analysis ($n = 191$). A final, necessary quality control measure was discovered during analyses. A small set of subjects ($n = 30$) had outlier residuals from log-log regression models[40–42] fit between total sulcal surface area (summed sulcal surface area from all 40 sulci) and total brain volume (Freesurfer's "BrainSegVol"). These subjects were visually confirmed to have been segmented poorly by FreeSurfer, leading to overestimation of sulcal surface area by BrainVISA. These subjects were also excluded from further analysis, leaving a final 34,725 subjects for analysis.

We considered additional cortical phenotypes measured adjacent to sulci for comparison in an inter-subject covariation analysis. Sulcal surface area and gray matter thickness were computed from the standard BrainVISA sulcal morphometry pipeline following merges of some sulcal labels. Gray matter volume, mean curvature, and gaussian curvature were measured along parcels from a sulcal parcellation in FreeSurfer fsaverage template space warped back to subject brains (https://github.com/willsnyder12/sulcal_phenotype_networks/tree/main/sulcal_parcellations) (see STAR Methods section "Structural and functional brain map annotation against SPNs").

Sulcal phenotype networks (SPNs)

SPNs were defined as the {40 x 40} matrix of correlations from {1 x 5} vectors of sulcal phenotypes between sulci in a given brain. First, sulcal phenotypes were extracted from subject scans in order to generate SPNs. Extracted sulcal medial walls contained points closest to the depths of sulci (bottom points, or fundus points) and points closest to the exterior of the brain, termed hull-junction points in BrainVISA as they lie along the hypothetical convex hull (inflated or unfolded surface) of the cortex (Figure 1A). Depth profiles or histograms (Figure 1B) were generated for any sulcus by finding the shortest geodesic path along the sulcal medial wall from fundus points to hull- junction points. Average depth was given by the median distance and depth variability was given by the median absolute deviation of distances, as in Klein et al.[39] We also explored the effect of substituting the normalized coefficient of variation (CV) in depth for the MAD metric of sulcal depth variability. We found these two metrics were positively correlated (r = 0.75) and the results of downstream network analyses were nearly identical regardless of whether we used MAD or CV to capture variation in sulcal depth (Figures S7A–S7C). We therefore used MAD for the principal analyses.

Exterior or hull-junction points were useful for branching pattern measures (longest branch, branch span, fractal dimension) as the full tangential sprawl of the sulcus is exposed at this minimum depth on the sulcal medial wall. Similar to length calculations native in BrainVISA, longest branch was defined as the longest contiguous geodesic path along hull-junction points given the same sulcal label. Branch span was inspired by analyses of dendritic morphology that used a "circularity index" to assess how uniform or dispersed the orientation of dendrites were about their soma.[38] This calculation is performed in a two-dimensional reference frame, so hull-junction points from contiguous sulcal branches were projected to a plane tangent to the hull of the cortex centered at the center of mass of a given sulcal branch. The sulcal branch point sets in the plane were all aligned to the center of mass of the largest sulcal branch if multiple sulcal branches were present. Branch span was given by the ratio of the convex hull area of this point set divided by its circumscribed area, as in Levy et al.[38] Circumscribed area was derived from the smallest enclosing circle of the point set (https://www.nayuki.io/page/smallest-enclosing-circle). Finally, fractal dimension was calculated from a three-dimensional box-counting algorithm (https://github.com/ChatzigeorgiouGroup/FractalDimension) applied to the hull-junction points all assigned a given sulcal label to assess self-similarity of sulcal branching patterns on the exterior of the cortex.

Age, sex, and TBV effects on sulcal phenotypes were modeled with multiple linear regression. Plots of each sulcal phenotype versus age and TBV were visually inspected and confirmed to have either linear or no relationship. Therefore, for consistency across the 200 linear models (40 sulci * 5 phenotypes), the same multiple linear regression model was used with linear terms for covariates. Bonferroni correction was performed for 120 tests (40 sulci * 3 covariates) to investigate significance within each model on a phenotype-by-phenotype basis.

All five sulcal phenotypes were calculated for all 40 bilateral sulci and for each subject to enable SPN generation. Each sulcal phenotype was Z-scored within each brain to capture within-brain inter-regional differences in sulcal phenotypes. Then, a {40 x 40} correlation matrix or SPN was generated by the sulcus pairwise correlation of the five sulcal phenotypes. Age, sex, and TBV effects on the 780 unique edges in the symmetric SPNs were modeled with multiple linear regression in the same manner as with individual sulcal phenotypes. Bonferroni correction was performed for 2,340 tests (780 edges by 3 covariates) to investigate significance within each model on an edge-by-edge basis.

Categorical and dimensional analyses of SPNs

Hierarchical clustering of group mean SPNs was performed in R (https://www.r-project.org/), finding an optimal split of the resulting dendrogram at two clusters, given by the number of clusters that maximized the Dunn index over 2 through 10-cluster solutions. The group-level eigen-fold index (EFI) was given by the first principal component of the full group mean SPN correlation matrix, assigning a PC loading to each sulcus, specifying low (negative) EFI scores to include linearly shaped sulci and high (positive) EFI scores to include more complex sulci. We chose to focus on the first PC as additional PCs accounted for substantially less (co)variance, had decreased interhemispheric consistency in PC loading, had increased inter-subject variability in subject-level PC loadings (Figure S7D), and were more prone to outlier PC loadings (Figure S7E). Group-level EFI was scaled from -1 to 1 for interpretability. The interpretation of linear and complex sulci was determined from viewing prototypical sulci across the PC loading space and by looking at sulcal phenotype distribution by sulcal cluster. For subject-level PCA decompositions, PC signs are arbitrary, so it would not be feasible to inspect and interpret all subject-level components. Additionally, subject-level PCs could each represent slightly different organizational axes. Therefore, subject-level EFI was calculated as sulcal coherence with the group-level EFI, calculated as the correlation between a subject SPN row for a given sulcus with the EFI.

Test-retest reliability of sulcal measures

We analyzed the multi-modal MRI reproducibility cohort[77] (https://www.nitrc.org/projects/multimodal/) from the Kennedy Krieger Institute (KKI) to assess reliability of sulcal measures. This cohort was selected so that we could benchmark the test-retest reliability of our sulcal metrics, and the SPN and EFI statistics derived from them, against the reliability of previously investigated sulcal morphometrics.[23] The KKI cohort of healthy subjects was scanned with T1 and T2 weighted acquisitions on a 3T scanner, comparable to the MRI protocol for the UK Biobank cohort.[77] We analyzed all available MRI data on 21 subjects (age 22-61 years, 11 males and 10 females) at baseline and follow-up assessments scheduled within 2 weeks of each other.[77] Each scan was processed in the same way as UK Biobank scans, using FreeSurfer, BrainVISA, and sulcal phenotype extraction pipelines. As in Pizzagalli et al.,[23] intraclass correlation (ICC) was used to assess test-retest reliability for the EFI and for each of the 5 sulcal phenotypes for each sulcus. The

upper triangle of individual subject-level SPNs was used to assess SPN identifiability, i.e., whether the SPN derived from a subject's follow-up scan was maximally correlated with the SPN derived from their baseline scan, compared to all SPNs derived from other subjects in the sample. Finally, Pearson's correlation between test-retest reliability of EFI (ICC) in the KKI cohort and between-subject variability of EFI (MAD) in the UK Biobank cohort was used to test the hypothesis that sulci with higher between-subject variation in the UK Biobank cohort might also have lower test-retest reliability in the KKI cohort.

Structural and functional brain map annotation against SPNs

Structural and functional maps comparable with EFI and SPN clusters were either derived from other studies or computed in the present study. Allometric scaling coefficients represented the degree to which two-dimensional sulcal surface area scaled with three-dimensional TBV, with values above 0.67 indicating positive allometric scaling (*i.e.*, more sulcal surface area than expected given TBV). Sulcal surface area was measured as in Fish et al.[40] for each sulcus, calculated as sulcus mean depth * length. Log-log regression models,[40–42] between age and sex residualized sulcal surface area and TBV (Freesurfer's ''BrainSegVol'', encasing volume of the cortex) were fit and had coefficients associated with total brain volume pulled for Pearson's correlation with EFI. The coefficients represented the degree to which sulcal surface area disproportionately increased with total brain volume increases.

Gray matter thickness measures for each sulcus and subject were computed by BrainVISA Morphologist, calculating thickness as the average geodesic distance from gray-white matter interface to the outer-most gray matter in volumetric space. Sampled points for each sulcus stretched from its fundus (bottom) through the sulcal bank up to the gyral peak (top), as defined by the volumetric parcellation BrainVISA generates (sulci Voronoi diagram) from sulcal labels.[43] Gray matter thickness values were averaged across subjects to allow Pearson's correlation with EFI.

Heritability estimates were derived from mega-analytic family-based studies using BrainVISA Morphologist to measure mean sulcal depth,[17] the measure most linked to the EFI in our study. Where heritability estimates were available for multiple sulcal labels that were merged into one label for the 40-sulcus parcellation used in this study, we used the maximum heritability (and corresponding standard error) of these sub-labeled sulci, since maximum values represented the most sensitive and meaningful sub-labeled sulci. Using the mean heritability of sub-labeled sulci did not considerably change significance or interpretation of the Pearson's correlation between mapped heritability values and EFI ($r = -0.63$, $P = 0.0094$).

Neurosynth meta-analytic functional annotation of SPNs, as performed in Wagstyl et al.,[50] used the Dice overlap between functional regions and regions of interest to infer functions subserved by the regions of interest. We generated a parcellation of sulcal regions in FreeSurfer's FreeView application (http://surfer.nmr.mgh.harvard.edu/) consistent with BrainVISA standard sulcal labeling[16] and endpoints of sulcal regions in the Destrieux atlas[82] or complex sulcal clusters with functional regions. All sulcal parcellations used in this study are to test for overlap between linear provided (https://github.com/willsnyder12/sulcal_phenotype_networks/). 30 functional regions were computed from 30 topic-modeling derived terms from over 11,000 functional MRI tasks (https://neurosynth.org).[44,69] Significant functional regions were downloaded (https://neurosynth.org/analyses/topics/v4-topics-50/), mapped to closest vertices on an average pial surface mesh, and tested for dice overlap with linear and complex sulcal regions.

Functional hierarchy was measured as the first principal component loadings of functional connectivity from Margulies et al.[45] and downloaded using NeuroMaps.[70] The difference in loadings between linear and complex sulcal regions was compared to a null distribution based on permuted linear and complex sulcal labels, asking whether this difference was more extreme than in randomly constructed SPN cluster definitions. Permuted labels were generated from spinning the original labels projected onto a sphere and reassigning labels to sulcal regions 10000 times, using the *gen_spinsamples* Python function from the *netneurotools* package with the Hungarian algorithm selected.[83]

Fetal cortical surface processing

Sulcal curvature was measured in each of 40 bilateral sulci for $n = 228$ subjects aged 21-36 weeks GA from the Developing Human Connectome Project's (dHCP) fetal imaging cohort. Fetal MRI were passed through the dHCP structural processing pipeline,[33] with initial tissue segmentation performed by DRAW-EM.[72] Quality control of T2-weighted images, segmentations, and surface reconstructions informed subsequent manual editing of tissue segmentations by expert (V.K.) for every subject. Edited segmentations were again passed through surface reconstruction to yield final surfaces.[84] Subjects with low quality assessment scores ($n = 5$) from expert evaluation were visually inspected to confirm poor quality and were excluded.

We annotated sulcal regions on a template fetal cortical surface and registered fetal cortical surfaces to templates to enable measurement of sulcal curvature along prospective sulcal regions annotated in alignment with adult sulcal parcellation. Coordinates of subject surfaces were aligned with nearest age templates created for surfaces 21- 36 weeks GA.[85] Surface alignment was performed using spherical representations of cortical surfaces, aligning dHCP subject maps of sulcal depth with template sulcal depth using Multimodal Surface Matching (MSM).[73,86] Aligning surfaces via sulcal depth to nearest-week spatiotemporal templates[87] has been found to be effective for fetal surface registration.[88] By computing vertex- wise averaging of curvature across subjects mapped to a given GA week template, we were able to visually inspect and confirm that MSM successfully aligned all major sulcal landmarks as expected (Figure 6A). Sulcal borders were delineated on the 36 weeks GA template in *FreeVie*w in alignment with BrainVISA standard sulcal labeling[16] and endpoints of sulcal regions in the Destrieux atlas[82] to allow comparison between BrainVISA sulcal measures from adults. All sulcal parcellations from our analysis are available at www.github.com/willsnyder12/sulcal-phenotype-networks. These borders were then mapped to each next earliest GA template successively using MSM and were visually assessed

for successful registration. As in Xu et al.,[46] the gray-white matter interface was used for measurement of cortical curvature.[89] Absolute values of the curvature in each sulcal region measured sulcation as the degree of deviation from a flat surface.

Following Xu et al.,[46] curvature along the grey-white matter interface surface can be cross- sectionally modeled along development using a Gompertz function. For all 40 bilateral sulci, we fit a Gompertz function using Python's *curve_fit* function as part of the SciPy *optimize* module. All models had an R-squared of approximately 0.8 or higher, except for two sulci (left intermediate frontal and right orbitofrontal) which were visually confirmed to have models that accurately portrayed sulcal emergence. Additionally, we visually compared each model against an animation (https://github.com/StuartJO/BrainSurfaceAnimation) created from temporal interpolation of template surfaces, again confirming that the models behaved in agreement with visually recognizable timing of sulcation (Videos S1 and S2). Gestational age at fitted values for 10% and 50% of the estimated plateau of Gompertz functions defined T_{10} and T_{50} sulcal development milestones, which were subject to Pearson's correlation against EFI. Additionally, a general additive model with 5 knots (optimized to balance over and under-fitting) was fit between T_{50} and the median absolute deviation of subject EFI scores for each sulcus using the *gam* function from the *mgcv* library in R.[90]

Transcriptional annotation of SPNs

We used the dense expression maps (DEMs) created in Wagstyl et al.[50] to test for sulcal alignment with gene expression gradients. Microarray gene expression for each of 20,781 genes was assessed in multiple different cortical locations from six postmortem donor brains from the Allen Human Brain Atlas.[52] The spatially smoothed and averaged maps were found to replicate other known cytoarchitectonic boundaries in Wagstyl et al.[50] In the present work, we first asked whether gradients of gene expression maps were greater in linear as compared to complex sulci, hypothesizing that gene expression would undergo more drastic changes about linear sulci. We again used spin-based permutations[83] with 1000 spins to evaluate evidence for greater gradient magnitude in linear sulci.

Post-hoc analysis tested whether specific linear sulcal fundi marked the distinct boundary between high and low cortical gene expression. Sulcal fundi can be determined for linear sulci in average mesh representations of the cortex due to their low inter-subject variability, so we first extracted linear sulcal fundi using Automated Brain Line Extraction (ABLE)[74] in MATLAB (https://www.mathworks.com). Resulting sulcal fundi lines were corrected for small errors by redrawing on the cortical surface using Connectome Workbench's image viewer.[75] The fundi represented the midline between gyral crests that traced through the points of highest curvature at the deepest points of sulci. Sulcal fundi and DEMs were both projected to spherical representation of the cortical surface, with gene expression gradients and sulcal fundus orientation recomputed on the sphere using the Workbench *-metric-gifti* command.[75] Principal expression vectors were calculated as the first principal component of gene expression gradient vectors at each vertex across all genes. To first test whether these vectors ran orthogonal to sulcal fundi at large magnitude, each sulcal fundus was scored with the following equation:

$$\frac{1}{n}\left(\sum_{i}^{n} m_i * sin(g_i, f_i)\right) \quad \text{(Equation 1)}$$

where n = number of vertices in a sulcal region, m_i = magnitude of the mean gradient at vertex i, $i = i^{th}$ vertex, g_i= gradient vector at vertex i, and f_i = fundus orientation vector for the closest fundus vertex to vertex i. For each sulcus, this value was recomputed following 10,000 random spins of the sulcal fundus about the sphere, ensuring the spun fundus did not cross into subcortical vertices. The degree to which all vectors pointed the same direction was not considered as the sign of the principal expression direction is arbitrary. For gene-level scores for each sulcus, the same score was used but also had to consider the degree to which all vectors pointed the same direction about the sulcal fundus, given by the equation:

$$\frac{1}{n}\left(\sum_{i}^{n} m_i * sin(g_i, f_i)\right) * \frac{1}{n}\left(\sum_{i}^{n} d_i\right) * d_o \quad \text{(Equation 2)}$$

where d_i was a binary variable representing the direction the gradient vector pointed to (*e.g.*, 0 = left-to-right through sulcal fundus and 1 = right-to-left through sulcal fundus when the majority of vertices had gradient vectors oriented right-to-left) and d_o(overall direction) was -1 or 1 depending on the direction the majority of vertices' gradient vectors pointed through the sulcal fundus. This calculated the strength of orthogonal gene expression gradient to sulcal fundi, weighted by the angle, amount of vectors pointing the same direction, and magnitude of gradient. Thus, signed gene scores gave information on the direction and coherence of the trans-sulcal alignment of gradient vectors with the sulcal fundus. Gene ontology enrichment for gene scores were computed using spatial permutation nulls, wherein the sulcal fundus was randomly rotated 10,000 times with gene scores recomputed for each rotation. As in Fulcher et al.,[91] the mean gene score for a gene category was tested for whether it was more extreme than mean gene scores from spatially permuted data. Bonferroni correction accounted for two sulci (significant from principal expression analysis) times two directions from which genes could transition from low to high or high to low expression.

Cross-sectional analysis of post-mortem gene-expression data was performed using the BrainSpan dataset (http://brainspan.org)[52] which included sparse samples from ages ~10 weeks (GA) to 40 years. Normalized gene expression data (http://development.psychencode.org/)[71] were interpolated using code from Stauffer et al.[76] and Warrier et al.[25] to visualize developmental trajectories of genes that demonstrated significant trans-sulcal gradients of expression orthogonal to the central sulcus.

QUANTIFICATION AND STATISTICAL ANALYSIS

All quantification and statistical analysis was performed in R (https://www.r-project.org/) and Python (https://www.python.org/). All relationships between sulci within subjects, across subjects, and with covariates were assessed in R with statistical tests as described above in method details. When comparing separate maps of regional sulcal morphology, we used linear models in R. When comparing sulcal morphology to dense, vertex-level data on the cortical surface, we used spatial permutation testing[83,91] in Python to account for spatial autocorrelation effects. Sample size and measures of spread are indicated either in the text of the results section or in figure captions. Significance was assessed at $P<0.05$ with correction for multiple corrections as specified above.